CHEMISTRY
A EUROPEAN JOURNAL

DOI: 10.1002/chem.200701396

VIP

The Mystery of Perpendicular Fivefold Axes and the Fourth Dimension in Intermetallic Structures

Robert F. Berger, Stephen Lee,* Jeffreys Johnson, Ben Nebgen, Fernando Sha, and Jiaqi Xu[a]

Abstract: The structures of eight related known intermetallic structure types are the impetus to this paper: $Li_{21}Si_5$, $Mg_{44}Rh_7$, $Zn_{13}(Fe,Ni)_2$, Mg_6Pd, Na_6Tl, $Zn_{91}Ir_{11}$, $Li_{13}Na_{29}Ba_{19}$, and $Al_{69}Ta_{39}$. All belong to the $F\bar{4}3m$ space group, have roughly 400 atoms in their cubic unit cells, are built up at least partially from the γ-brass structure, and exhibit pseudo-tenfold symmetric diffraction patterns. These pseudo-tenfold axes lie in the ⟨110⟩ directions, and thus present a paradox. The ⟨110⟩ set is comprised of three pairs of perpendicular directions. Yet no 3D point group contains a single pair of perpendicular fivefold axes (by Friedel's Law, a fivefold axis leads to a tenfold diffraction pattern). The current work seeks to resolve this paradox. Its resolution is based on the largest of all 4D Platonic solids, the 600-cell. We first review the 600-cell, building an intuition discussing 4D polyhedroids (4D polytopes). We then show that the positions of common atoms in the $F\bar{4}3m$ structures lie close to the positions of vertices in a 3D projection of the 600-cell. For this purpose, we develop a projection method that we call intermediate projection. The introduction of the 600-cell resolves the above paradox. This 4D Platonic solid contains numerous orthogonal fivefold rotations. The six fivefold directions that are best preserved after projection prove to lie along the ⟨110⟩ directions of the $F\bar{4}3m$ structures. Finally, this paper shows that at certain ideal projected cluster sizes related to one another by the golden mean ($\tau=(1+\sqrt{5})/2$), constructive interference leading to tenfold diffraction patterns is optimized. It is these optimal values that predominate in actual $F\bar{4}3m$ structures. Explicit comparison of experimental cluster sizes and theoretically derived cluster sizes shows a clear correspondence, both for isolated and crystalline pairs of projected 600-cells.

Keywords: higher dimension · intermetallic phases · polytopes · solid-state structures · X-ray diffraction

Introduction

Consider the enigma of complex intermetallic crystal structures, thermodynamically stable atomic arrangements with hundreds or even thousands of atoms within the unit cell. Characteristic examples are $Li_{21}Si_5$, $Mg_{44}Rh_7$, and $Al_{69}Ta_{39}$, compounds that crystallize in the $F\bar{4}3m$ space group, with large numbers in their stoichiometric ratios and correspondingly large unit cells. Is there some pattern to these complex crystal structures that eludes the casual observer, but which can explain essential features of their structures?

In this paper we will uncover one such pattern. The starting point will be diffraction. We shall find that the diffraction patterns of the above structures contain a pseudo-tenfold symmetry with an attached paradox. The mystery will not be that tenfold diffraction symmetry is incompatible with crystalline symmetry; that peculiarity has already been explored in the context of quasicrystal approximants.[1] The paradox we refer to is a simpler one.

The compounds $Li_{21}Si_5$, $Mg_{44}Rh_7$, and $Al_{69}Ta_{39}$ all adopt cubic crystal structures with pseudo-fivefold symmetry along the [110] direction. In cubic symmetry, the [110] direction has five other symmetry-equivalent directions. These compounds therefore have pseudo-fivefold symmetry axes along [110], [1$\bar{1}$0], [011], [01$\bar{1}$], [101], and [10$\bar{1}$]: three pairs of perpendicular pseudo-fivefold axes. The paradox is that no three-dimensional point group contains a single pair of perpendicular fivefold symmetry axes, let alone three such pairs.

[a] R. F. Berger, Prof. S. Lee, J. Johnson, B. Nebgen, F. Sha, J. Xu
Department of Chemistry and Chemical Biology
Cornell University, Ithaca, NY 14853-1301 (USA)
Fax: (+1) 607-255-4137
E-mail: sl137@cornell.edu

Supporting information for this article is available on the WWW under http://www.chemeurj.org/ or from the author.

The solution to this paradox is simple yet unexpected. While there are no three-dimensional (3D) point groups with perpendicular fivefold symmetries, there are four-dimensional (4D) point groups with orthogonal fivefold symmetries. The common atomic sites of these $F\bar{4}3m$ structures prove to be connected to one such 4D point group. We will show that the common atomic sites of $Li_{21}Si_5$, $Mg_{44}Rh_7$, and $Al_{69}Ta_{39}$ lie at the 3D-projected points of a very symmetrical 4D object. It is this 4D object that has exact orthogonal fivefold symmetries. Of course, these fivefold symmetry operations are no longer exact once projected into 3D space; however, after projection, enough of their fivefold symmetry is retained that a pseudo-tenfold symmetric diffraction pattern (tenfold due to the pseudo-fivefold symmetry coupled with Friedel's Law[2]) is observed even in three dimensions.

This paper therefore begins with the observation of pseudo-tenfold diffraction symmetry in the aforementioned crystal structures. It then examines those atoms in these crystal structures principally responsible for the observed pseudo-tenfold diffraction symmetry.

At this point we begin our analysis of 4D objects. We will show that 4D objects can be understood through 3D images of them, in much the same way that ordinary two-dimensional (2D) images are used to understand 3D solids. We will therefore consider 3D images of a particular 4D object—an object with perpendicular fivefold symmetry. We show that this object, once projected into 3D space, retains a pseudo-tenfold diffraction symmetry.

We find that at certain ideal configurations and sizes, these diffraction images are optimal. Connecting these mathematical ideas to the actual reality of the true $Li_{21}Si_5$, $Mg_{44}Rh_7$, and $Al_{69}Ta_{39}$ crystal structures, we find that the atoms of these crystal structures lie near sites of the projected 4D object, and therefore exhibit pseudo-tenfold diffraction symmetry. At the same time, they have interatomic distances that optimize constructive interference in their diffraction patterns.

The story we create builds upon the observations of others. While the types of structures we describe—intermetallic crystal structures with regions consisting entirely of close-packed, slightly distorted tetrahedra—have a rich history of efforts to catalogue and systematize their geometries,[3–9] we will mention only the observations most directly relevant to this paper. First among these was the realization by Samson and co-workers[10–13] that large cubic intermetallic structures such as $NaCd_2$ and Cd_3Cu_4 contain a pseudo-fivefold symmetry perpendicular to their crystallographic $\langle 1\,1\,0\rangle$ directions. This same pseudo-fivefold symmetry was later observed by Khare and co-workers[14] for the γ-brass structure, and it was pointed out that the axes were inconsistent with those in known quasicrystals and quasicrystal approximants.[1] Later came the observation by Nyman, Andersson, Hyde, and others[17,18,19] that the γ-brass structure, among other tetrahedrally close-packed structures, is one in which the edge-capped stella quadrangula plays a central role. (We review the edge-capped stella quadrangula later in this paper for readers unfamiliar with it.) And finally, there is the more recent work of Sadoc and Mosseri,[20,21] who recognized that the fundamental clusters of structures such as Cr_3Si, α-Mn, and γ-brass bear a clear relationship with the 4D Platonic solid, the 600-cell. All of these observations are fundamentally connected and, as we hope to show for the $Li_{21}Si_5$, $Mg_{44}Rh_7$, and $Al_{69}Ta_{39}$ structures, tell different aspects of a single unified story.

[1] Although there are differences between the $\langle 1\,1\,0\rangle$ and $\langle 1\,\tau\,0\rangle$ directions, Dong and others[15,16] have analyzed the relationships between γ-brasses and approximants of icosahedral and decagonal quasicrystals.

Results and Discussion

Large $F\bar{4}3m$ intermetallic structures

Description of their structures: Seven structure types listed in Pearson's Handbook of Crystallographic Data for Intermetallic Compounds[22] in the space group $F\bar{4}3m$ contain approximately 400 atoms in their unit cells. Compounds for which X-ray single crystal data sets have been recorded and solved include $Li_{21}Si_5$,[23,24] $Zn_{21}Pt_5$,[25,26] $Cu_{41}Sn_{11}$,[27,28] $Mg_{44}Rh_7$,[29] $Zn_{39}Fe_{11}$,[30] $Mg_{44}Ir_7$,[31] $Zn_{13}(Fe,Ni)_2$,[32] Mg_6Pd,[13] $Mg_{29}Ir_4$,[33] Na_6Tl,[12] $Zn_{91}Ir_{11}$,[34] $Li_{13}Na_{29}Ba_{19}$,[35] and $Al_{69}Ta_{39}$.[36] To varying degrees, these structure types are all based on a simpler parent structure, γ-brass.[37] In this paper we will restrict our attention to the above 13 solved crystal structures. (Of a total of 15 known to us, these 13 bear the simplest connection to the γ-brass structure.) We review the essential features of this simpler structure first.

The γ-brass structure is illustrated in Figure 1a. The structure is a cubic *I*-centered arrangement of the 26-atom cluster shown in this figure, a cluster composed of four distinct sites: IT (inner tetrahedron), OT (outer tetrahedron), OH (octahedron), and CO (cuboctahedron). In accord with the *I*-centering condition, there are two of these 26-atom clusters per cubic unit cell.

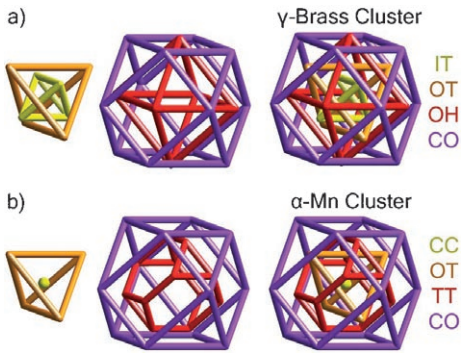

Figure 1. Two atomic clusters common to the $F\bar{4}3m$ intermetallic structures: a) the 26-atom γ-brass cluster and b) the 29-atom α-Mn cluster. Clusters are shown as nested polyhedra, with each crystallographic site represented by a color (inner tetrahedron (IT) or cluster center (CC): yellow; outer tetrahedron (OT): orange; octahedron (OH) or truncated tetrahedron (TT): red; and cuboctahedron (CO): purple).

The simplest of the large unit-celled $F\bar{4}3m$ structures, $Li_{21}Si_5$, $Zn_{21}Pt_5$, and $Cu_{41}Sn_{11}$, are $2\times2\times2$ ordered superstructures of γ-brass. The *a*, *b*, and *c* axes of these crystals are each twice as long as the corresponding axis length in γ-brass; these crystals' unit cells therefore have eight times the volume of γ-brass. Instead of two 26-atom clusters per unit cell, there are 16.

All of these structures are *F*-centered, which requires each cluster to have three translationally equivalent clusters, and hence these 16 clusters can be reduced to four translationally inequivalent ones. In the space group $F\bar{4}3m$, these four clusters are also not related by any point-group operation. They are all crystallographically unique.

Specifying the atomic site positions (and the atom types) of these four clusters identifies these structures. In Figure 2,

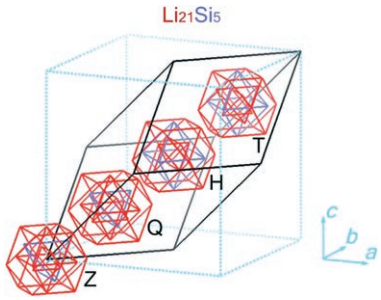

Figure 2. The four crystallographically inequivalent γ-brass clusters in $Li_{21}Si_5$ (Li: red; Si: blue), shown in both the primitive unit cell (black) and the cubic unit cell (cyan). The clusters are centered in the cubic cell at Z (0,0,0), Q ($\frac{1}{4},\frac{1}{4},\frac{1}{4}$), H ($\frac{1}{2},\frac{1}{2},\frac{1}{2}$), and T ($\frac{3}{4},\frac{3}{4},\frac{3}{4}$).

we show the four crystallographically inequivalent clusters of $Li_{21}Si_5$. The four clusters lie inside a single primitive unit cell. As this picture further shows, the four inequivalent clusters lie in a cubic cell at (0,0,0), ($\frac{1}{4},\frac{1}{4},\frac{1}{4}$), ($\frac{1}{2},\frac{1}{2},\frac{1}{2}$), and ($\frac{3}{4},\frac{3}{4},\frac{3}{4}$). We will refer to these four clusters as the Z, Q, H, and T clusters, the clusters being at zero, a quarter, a half, and three-quarters of the cell dimension, respectively.

As Figure 2 shows, differences exist between the four clusters: in $Li_{21}Si_5$, the Si atoms occupy different positions in the different clusters (for the Z and Q clusters the Si atoms lie on the OT sites, while for the H and T clusters they lie on the OH sites).[2] However, in the $F\bar{4}3m$ family of structures, clusters can differ to an even greater extent. Clusters can have radically different atomic sites. One such different cluster is illustrated in Figure 1b. This cluster, found in $Zn_{91}Ir_{11}$, does not have any atoms at either the IT or OH sites, but instead has atoms at the center of the cluster (CC) and in a truncated tetrahedron (TT). This new cluster type is generally referred to as an α-Mn cluster, due to its similarity to the principal constituent cluster of that structure type.[38]

[2] In addition, there is an interesting variation among the orientations of the various clusters in $Li_{21}Si_5$. As careful examination of Figure 2 shows, the orientation of the inner tetrahedron of the H cluster is inverted with respect to the orientations of the Z, Q, and T clusters.

Other cluster types with descriptive names such as Ti_2Ni, bcc, and fcc (so named because of clear connections to these parent structures) also exist.[3] However, all cluster types are composed of just the six aforementioned types of atomic sites (CC, IT, OT, OH, TT, and CO). There are always four crystallographically inequivalent clusters located at Z, Q, H, and T. All sites can therefore comfortably be labeled with a three-letter designation: for example, HTT would refer to a truncated tetrahedral site centered at ($\frac{1}{2},\frac{1}{2},\frac{1}{2}$). In this article, these three-letter designations will prove more useful than the traditional names based on descriptive names such as α-Mn or Ti_2Ni.

In this paper, we will consider eight structure types (as we shall see, our definition of structure type will be slightly different from the standard definition). We will consider only those structures that are traditionally considered to contain a γ-brass cluster. This includes 13 of the 15 $F\bar{4}3m$ $2\times2\times2$ compounds known to us for which a single-crystal structure has been solved.[4]

Pseudo-tenfold diffraction along the [1$\bar{1}$0] direction: In Figure 3, we show single-crystal X-ray diffraction images[42] for two of the $F\bar{4}3m$ family of structures, $Zn_{39}Fe_{11}$ and $Na_{29}Li_{13}Ba_{19}$. (We have chosen these two structures as they are the two structures where pseudo-tenfold symmetry is strongest, but as the Supporting Information illustrates, pseudo-tenfold diffraction is present in the remaining members of the family.) In Figure 3, we show reflections orthogonal to the [1$\bar{1}$0] direction. We show only the most intense peaks.

The diffraction images of Figure 3 exhibit a pseudo-tenfold symmetry. Diffraction spots appear in two distinct rings. For the inner ring, strong reflections include 660, 555, and 228; for the outer ring, they include 10100, 888, and 3313. These *hkl* indices belong to an understandable general pattern related to the Fibonacci sequence.

Recall in the Fibonacci sequence (1, 1, 2, 3, 5, 8, 13,…), each number is the sum of the two previous numbers of the sequence. Let us call a given Fibonacci sequence number h_i, the numbers preceding and following this number then being $h_{i\pm1}$. Consider now the set of *hkl* reflections, $(2h_i,2h_i,0)$, $(h_{i+1},h_{i+1},h_{i+1})$, and $(h_{i-1},h_{i-1},h_{i+2})$ (we use commas and parentheses here for the sake of clarity). The rings of peaks previously mentioned then correspond to the sets in which h_i are 3 and 5, respectively. (For example for $h_i=3$, these peaks correspond to $(2h_i,2h_i,0)=660$, $(h_{i+1},h_{i+1},h_{i+1})=555$, and $(h_{i-1},h_{i-1},h_{i+2})=228$.) The connection to the Fibonacci sequence will prove to run deeper than the

[3] These alternate names are important in their own right. We have recently shown, for example, that the Ti_2Ni cluster plays a fundamental role in understanding quantum calculations on the $Mg_{44}Rh_7$ structure.[39]

[4] The remaining two structures, $Zn_{20.44}Mo$[40] and $Cd_{45}Sm_{11}$,[41] contain clusters based on the body-centered cubic (bcc) structure. While the ideas of this paper can be applied to the remaining two structures (recall that γ-brass is itself a defect bcc structure), the inclusion of these structures would require several multipage excursions, of a length suited perhaps for another full article.

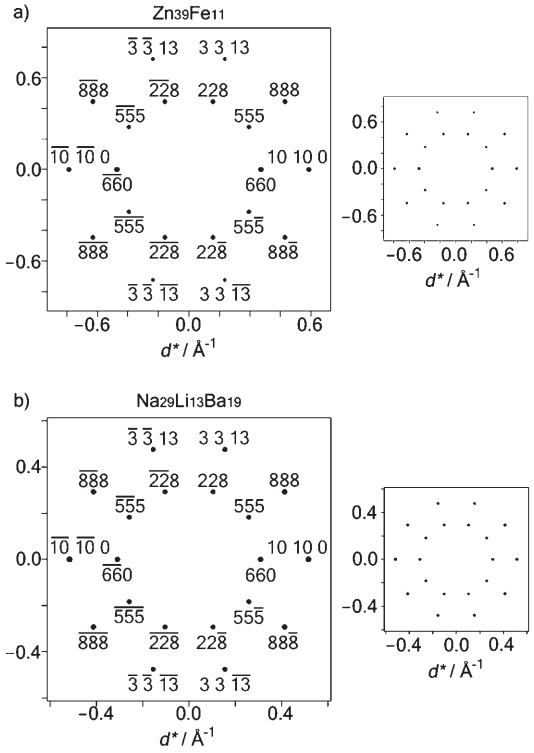

Figure 3. Simulated single-crystal X-ray diffraction patterns of a) $Zn_{39}Fe_{11}$ and b) $Na_{29}Li_{13}Ba_{19}$, viewed in the $[1\bar{1}0]$ direction. Only the brightest peaks are shown: they exhibit a striking pseudo-tenfold symmetry. As all the strongest reflections are normal to the $\langle 1\,1\,0\rangle$ directions, this figure reveals all the most intense peaks of these structures. See Table 1.

above observations, but in order to appreciate these connections we will need a number of additional concepts.

How is it that different structure types with differing atomic positions can all exhibit pseudo-fivefold symmetry? A suggestive clue to the answer to this question is given in Table 1, which lists relative intensities of the six most intense symmetry-inequivalent diffraction peaks of $Zn_{39}Fe_{11}$ and $Na_{29}Li_{13}Ba_{19}$. These peaks belong to the two previously discussed rings of pseudo-tenfold diffraction. As this table shows, peaks within a given ring are not uniform in intensity. This lack of uniformity provides a measure of the incompleteness of the tenfold symmetry.

Table 1. Strongest X-ray reflection intensities. Diffraction data calculated by Cerius2[42] for $Cu_{K\alpha}$ radiation for 2θ ranging from 0 to 110°. The $Li_{13}Na_{29}Ba_{19}$ 16 16 0 reflection is among the most intense peaks. It corresponds to the third ring in which $h_i = 8$. See text.

$Zn_{39}Fe_{11}$			$Li_{13}Na_{29}Ba_{19}$		
Reflection	All atoms	Common sites	Reflection	All atoms	Common sites
6 6 0	100	100	6 6 0	79	94
5 5 5	40	50	5 5 5	52	58
2 2 8	54	65	2 2 8	55	61
10 10 0	67	84	10 10 0	100	100
8 8 8	58	72	8 8 8	78	88
3 3 13	22	33	3 3 13	59	71

In this same table, we also give the calculated intensities using only those atomic positions shared across the full family of $F\bar{4}3m$ structures (there are 12 such positions). Restricting the diffraction pattern to these common atoms improves the uniformity in diffraction intensities: it also improves overall pseudo-tenfold symmetry. Not shown, but equally true, is that this restriction improves the diffraction symmetry of the full family of $F\bar{4}3m$ structures. We therefore conclude that the origin of the pseudo-tenfold symmetry lies in the common atoms.

Trying to understand the common atoms brings us to the heart of this paper. It is a heart that involves geometrical concepts of a sort not familiar to most of us. The very perpendicularity of the pseudo-fivefold axes, coupled with the absence of any 3D point group with perpendicular fivefold axes, forces unusual geometrical concepts upon us.

We shall see that the key idea will be the introduction of a fictitious fourth dimension. This fourth dimension will have a number of concrete uses. It will allow us to create perpendicular fivefold axes that perfectly align with the $\langle 1\,1\,0\rangle$ directions of these crystals. It will also allow us to create a continuous array of perfectly regular face-sharing tetrahedra, a geometrical array which many of us know cannot be achieved in three dimensions.

Four-dimensional (4D) Platonic solids

Projected views of three-dimensional (3D) Platonic solids: The 4D geometry we will use is connected to 4D Platonic solids. Such 4D Platonic solids may seem at first a forbidding topic, but as we hope to show, many of the same tricks used to understand 3D Platonic solids can be applied to 4D Platonic solids. In particular, we note that much of our understanding of 3D objects is based on 2D pictures of them. We have trained ourselves to look at these 2D pictures and convert them in our minds into 3D solids. In exactly the same way, in this article we will consider 3D images of 4D solids and use our minds to turn these 3D images into representations of a true 4D object.

We begin by considering ordinary 3D Platonic solids, 3D polyhedra in which all vertices, edges, and faces are identical. In this article, we consider four of the five 3D Platonic solids: the tetrahedron, the octahedron, the dodecahedron, and the icosahedron. These Platonic solids are illustrated in Figure 4. The tetrahedron is of T_d point-group symmetry, the octahedron of O_h symmetry, and the dodecahedron and icosahedron of I_h symmetry. Furthermore, the dodecahedron and icosahedron are duals of each other: atoms placed at the center of the faces of one polyhedron lie at the vertices of the other polyhedron.

We begin our account by carefully considering the views of these Platonic solids along their symmetry axes. (As we shall see, 4D Platonic solids are also most clearly viewed down their symmetry axes.) In Figure 5, we show the octahedron down its fourfold axis and the dodecahedron down its

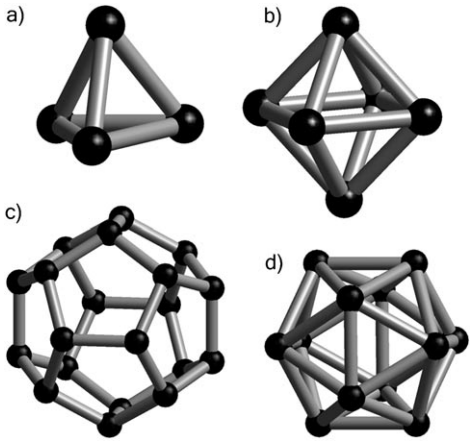

Figure 4. Four of the five 3D Platonic solids: the a) tetrahedron, b) octahedron, c) dodecahedron, and d) icosahedron.

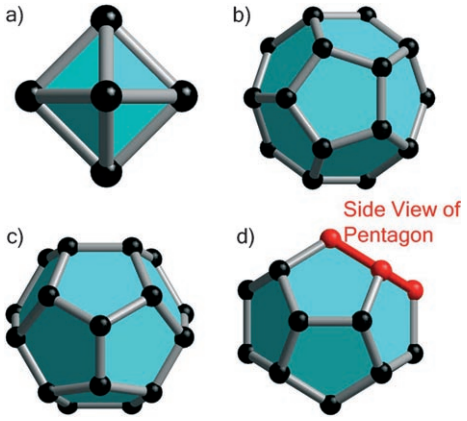

Figure 5. Various 3D polyhedra viewed down their symmetry axes. a) An octahedron viewed down its fourfold axis, and a dodecahedron viewed down its b) fivefold, c) threefold, and d) twofold axes (with a pentagonal face that appears as a line segment shown in red).

five-, three-, and twofold axes. Each of these views will teach us general principles useful in understanding 4D solids.

We begin with the octahedron. The octahedron is composed of six vertices and eight faces, but only five of its vertices and four of its faces are visible in Figure 5. The reason is evident; upon projection into the plane of the picture, half of the polyhedron is obscured by the other half.

We may view this missing half from two very different viewpoints. If we are to view Figure 5a as a picture of a real 3D octahedron, we then assume that the other half of the octahedron is hidden from view, but actually exists as the underside of the polyhedron. Equally relevant, however, is another more 2D perspective. Imagine that Figure 5a actually represents a true 2D object (a 2D object created by projecting the 3D octahedron into the 2D space). From this viewpoint, only one-half of the 3D octahedron has been successfully projected into 2D space. The other half cannot be successfully projected as this would force vertices to be projected into the interior of the first half. If vertices are to become atoms, such a mapping would place atoms at chemically unreasonable distances with respect to other atoms.

A similar distinction will take place with 3D projections of a 4D Platonic solid. In some cases, vertices will be present, but hidden by the upper side of the 3D polyhedron. In other cases, some atoms will not be projected, as such projection would place the new atoms into the interior volume already occupied by other projected atoms. In this paper, we will refer to the former as vertices (or atoms) hidden from view, and the latter as atoms in the shadow of other atoms.

Further important features can be extracted from the three views of the dodecahedron. We begin with the fivefold view, Figure 5b. Just 15 of the vertices and six of the faces of the dodecahedron can be seen in this view. Of the six visible pentagons, only the central pentagon appears perfectly regular, while the remaining five take on a somewhat compressed shape (although in the 3D polyhedron, they are just as regular as the central pentagon).

The compressed aspect of the outer pentagons has two components to it. First, the projected area of the compressed pentagons is smaller than that of the central pentagon. Second, the edges of the polyhedron that lie at the sharpest angle with respect to the plane of the picture are somewhat shorter in appearance. Both components will later prove important in understanding 4D Platonic solids.

The threefold view of the dodecahedron, Figure 5c, tells a similar story. Only six of the pentagonal faces are visible, the central three of which take on a distinctly more regular appearance than the outer three, the outer three pentagons having both significantly less area and (as some of the outer pentagons' edges are fairly perpendicular to the plane of the picture) significantly shortened edge lengths.

Of especial interest is the dodecahedron viewed down the twofold axis, Figure 5d. At first glance only four of the pentagonal faces can be seen, the central two of which take on the most regular appearance. In this view, however, there are four additional pentagonal faces that lie at the periphery of the projected view. These additional four pentagons are exactly orthogonal to the plane of the paper. The projected area of these pentagons is exactly zero; these four perpendicular polygons take on the appearance of line segments. (For the sake of clarity, one of these orthogonal pentagons is shown in red in Figure 5d.)

In this view, there are four additional faces that lie completely hidden by the visible faces. The number of hidden faces exactly equals the number of visible faces. This equality is not an accident. A dodecahedron has inversion symmetry. Upon inversion, the visible faces switch places with the hidden faces. The four peripheral faces that appeared as simple line segments in Figure 5d are equally pertinent here. The centers of the four peripheral faces lie exactly halfway between the visible and the hidden faces. If we were to use the terminology of a sphere, the four visible faces lie in one hemisphere, the four hidden faces in the other hemisphere, and the center of the four peripheral faces lie exactly on the equator.

We see finally one additional point that will later prove useful in understanding 4D solids. Whenever the direction of the projection is perpendicular (i.e., normal) to a given face, the given face preserves its symmetry upon projection. Thus, the fivefold view of the dodecahedron in Figure 5 is exactly normal to the central pentagonal face of the projection. It is therefore only in this fivefold view that the pentagonal symmetry of the original dodecahedron is perfectly preserved.

Identical vertices, edges, faces, and polyhedra: Before giving actual 3D images of 4D solids, we need to make some general observations about 4D Platonic solids. Our observations begin with lower-dimensional Platonic solids: regular polygons and regular polyhedra. Regular polygons are 2D objects with identical vertices (which are 0D) and identical edges (which are 1D). For 3D regular polyhedra, there is the additional requirement of identical faces (which are 2D). The salient point here is that in moving from 2D polygons to 3D polyhedra, we have added just one new component to our geometric description, the face, and that this new component is of one higher dimension than the highest dimension of the remaining components (the vertices and the edges).

It should therefore not be surprising that 4D Platonic solids will consist of identical vertices (0D), edges (1D), faces (2D), *and* polyhedra (3D). The polyhedra which are the constituent parts of a 4D solid are traditionally referred to as cells. (The 4D solids themselves are called 4D polytopes or polyhedroids.[43,44]) There are just six 4D Platonic solids,[45,46] of which three will be discussed in this article.

We may approach our understanding of 4D Platonic solids in a second, we hope, intuitive manner. Again, intuition needs to be based on our understanding of lower-dimensional Platonic solids. A 2D Platonic solid, a regular polygon, is composed of vertex-sharing (vertices are 0D) line segments (lines are 1D) that are each canted with respect to each other and which wrap together around an area (an area is 2D). A 3D Platonic solid is composed of edge-sharing (edges are 1D) polygons (polygons are 2D) that are canted with respect to each other and which wrap together around a volume (a volume is 3D). By analogy, we infer a 4D Platonic solid is composed of face-sharing (faces are 2D) polyhedra (polyhedra are 3D) that are canted with respect to each other and which wrap around a (fictitious) hypervolume (the hypervolume being 4D).

The 16-cell: The eight points $(\pm1,0,0,0)$, $(0,\pm1,0,0)$, $(0,0,\pm1,0)$, and $(0,0,0,\pm1)$ prove to be the vertices of one of the six 4D Platonic solids. Each of these points can be thought of as a 4D vector. Distances between pairs of vertices are therefore readily calculable. Each vertex has six nearest neighbors (for simplicity we shall say nearest-neighbor vertices are bonded to one another): for example, the point (1,0,0,0) has the six points $(0,\pm1,0,0)$, $(0,0,\pm1,0)$, and $(0,0,0,\pm1)$ at a distance of $\sqrt{2}$ away from it. As there are eight vertices, six bonds per vertex, and each bond is shared by two vertices, there are 24 bonds $(24=(8\times6)/2)$ in this polyhedroid (4D solid).

Both vertices of a pair of nearest neighbors (e.g., (1,0,0,0) and (0,1,0,0)) are mutually bonded to exactly four other vertices (in this case, $(0,0,\pm1,0)$ and $(0,0,0,\pm1)$). As each of these last four vertices is bonded to both of the originally bonded atoms, there are therefore four triangles of bonded atoms. The original bond lies simultaneously on four triangular faces. As there are 24 bonds, four triangles that share a common bond, and as a triangle is always composed of three bonds, there are 32 triangular faces $(32=(24\times4)/3)$ in this polyhedroid.

Consider one triangle of bonded atoms (e.g., (1,0,0,0), (0,1,0,0), and (0,0,1,0)). There prove to be exactly two vertices that are bonded to all three vertices of a bonded triangle. In the current example, the pair of vertices at $(0,0,0,\pm1)$ are both bonded to all three vertices of the triangle. Either of these last vertices, together with the initial triangle of bonded vertices, forms a tetrahedron. There are therefore exactly two tetrahedra that share a common triangular face. As there are 32 triangular faces, two tetrahedra that share a common face, and as a tetrahedron always has four faces, there are 16 tetrahedra $(16=(32\times2)/4)$ in this polyhedroid.

It will also prove useful to know the number of tetrahedra that share a common vertex. To calculate this number, we note that (the number of vertices)$\times$(the number of tetrahedra which share a given vertex)/(the number of vertices per tetrahedron)=the number of tetrahedra in the polyhedroid. There are eight vertices in the polyhedroid, four vertices per tetrahedron, and 16 tetrahedra in the 4D solid. Applying the above formula we find $8\times n/4=16$, in which n equals the number of tetrahedra that share a common vertex. We therefore find that the number of tetrahedra which share a common vertex is eight.

In summary, every vertex is shared by eight tetrahedra, every bond is shared by four triangles, and every face is shared by two tetrahedra. In addition, the number of vertices is eight, edges (or bonds) 24, faces (or triangles) 32, and cells (or tetrahedra) 16. These last numbers obey the 4D Euler relation:[46] (number of vertices)$-$(number of edges)$+$(number of faces)$-$(number of polyhedra)$=0$, as $8-24+32-16=0$. All vertices, edges, faces, and polyhedra (cells) are identical. The object described above is therefore a 4D Platonic solid. It is commonly referred to as the 16-cell, as it is composed of 16 tetrahedral cells.

Three-dimensional (3D) projections of the 16-cell: We now show our first picture of the 16-cell. Our picture will be a 3D projection of this 4D polyhedroid. Our picture perforce will be two-dimensional (2D) in nature, but unlike many literature pictures, will be based on standard 3D crystal graphics packages. Chemists are so experienced at viewing the output of 3D crystal graphics packages, we will be able to consider these pictures as being 3D in nature. (As a further aid, we include stereograms of some of these same pictures in the Supporting Information.) It will therefore be easy to envision these pictures as representing 3D-projected solids,

and furthermore to recognize that the projected vertices and edges could be seen as actual atomic site positions and bonds.

To create a 3D-projected image of the 4D 16-cell, we need to decide upon the direction (or view) of the projection. We will use the symmetry of the 16-cell coupled with insights based on 2D projections of 3D solids to guide our choice. Consider again the fivefold view of the dodecahedron, Figure 5b. We can think of this view as emanating from the choice of the central pentagonal face of this figure. As this pentagon is 2D, exactly one dimension less than the complete dodecahedron, this face is normal to a unique perpendicular axis. As Figure 5 shows, if we choose a projected view that is along this perpendicular axis, the fivefold symmetry remains perfectly preserved even after projection.

We use this same technique for the 16-cell. In this case, we need to consider not just a central 2D face, but a central 3D cell (polyhedron). In 4D space, there will be a unique direction perpendicular to the 3D space defined by this cell. We can choose this direction as the direction of projection. We will therefore choose one of 16 tetrahedra in the 16-cell to be the central cell, and choose the direction of projection to be perpendicular to this tetrahedron. By analogy to the preserved fivefold symmetry of the dodecahedron in Figure 5b, this projected 3D image of the 4D 16-cell will preserve the symmetry of the central tetrahedron.

In Figure 6, we show this projected view. We choose for this illustration a view that places the central tetrahedron

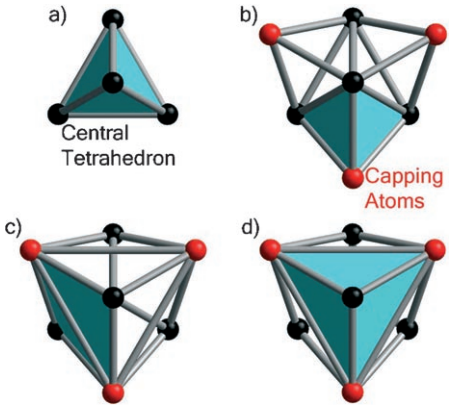

Figure 6. A T_d 3D projection of the 16-cell. a) The central tetrahedral cell. Central tetrahedron with b) face-sharing, c) edge-sharing, and d) vertex-sharing tetrahedra highlighted in cyan. Central tetrahedral vertices: black; capping tetrahedral vertices: red spheres. Capping vertices are slightly displaced for the sake of clarity (see Appendix).

along its threefold axis, Figure 6a. Recall that each triangular face of the 16-cell is shared by two tetrahedra. Thus each of the triangular faces must belong to a second tetrahedron besides the central tetrahedron. These second tetrahedra can be seen by placing an additional capping atom on each of the triangular faces of the initial tetrahedron.

One of the triangular faces of the central tetrahedron is hidden from view by the other triangles. Down the threefold view, its capping atom will not be visible; however, the three remaining capping atoms will be visible and are shown in Figure 6b. Each of these capping atoms taken together with their neighboring triangle of bonded vertices forms an additional requisite tetrahedron. These tetrahedra are somewhat compressed (this is especially clear in the stereograms in the Supporting Information). We can understand this compression in light of our earlier observation, that as one proceeds away from the center of the projection, faces and cells often become more and more compressed.

The four central tetrahedral atoms together with the four capping atoms make a total of eight atoms. As described in the last section, there are exactly eight atoms in the 16-cell. We have therefore considered all the vertices of this polyhedroid; however, we have not as yet considered all the tetrahedral cells.

Additional tetrahedra can be found betwixt the seven visible vertices of Figure 6b. There are four such tetrahedra. Three of these new tetrahedra emanate from a pair of atoms of the central tetrahedron coupled with a pair of the capping atoms (these new tetrahedra are edge-sharing with respect to the central tetrahedron), Figure 6c. A final tetrahedron is formed by a central tetrahedral atom (the one at the center of the picture) together with all three of the visible capping atoms, Figure 6d. All these additional tetrahedra are compressed after 3D projection.

There are therefore eight tetrahedra to be found in Figure 6 ($8=1+3+3+1$). All eight of these tetrahedra have the central atom of the threefold projection as one of their constituent atoms. We recall from the last section that every vertex is shared by exactly eight tetrahedra. Figure 6 therefore illustrates all the tetrahedra that share the central atom of the threefold projection.

There are of course 16 tetrahedra in the 16-cell. Only eight of its tetrahedra are seen in Figure 6. The reason for this can be traced to the lone capping atom that lies hidden from view by the other atoms. As this lone atom is also shared by eight tetrahedra, there must be eight tetrahedra not visible in Figure 6. These eight missing tetrahedra, together with the eight tetrahedra which we have previously described, account for all 16 tetrahedra of this polyhedroid.

The projected 120-cell: We now consider 4D Platonic solids that contain fivefold symmetry. It may come as no surprise that such polyhedroids are 4D analogues of the dodecahedron and the icosahedron. We begin with a 4D Platonic solid that contains dodecahedral cells. The actual coordinates of this solid are given in the Supporting Information. Here we will simply describe a 3D projection of this polyhedroid. As the polyhedroid we are about to describe is composed of 120 identical dodecahedra, it is traditionally referred to as the 120-cell.

Recall that in making a projection, we need to choose a direction of projection. We choose this direction in the canonical way, by designating one of the dodecahedra of the 120-cell the central one, and finding the direction perpendicular to this dodecahedron. This projection, as well as the 3D

coordinates it generates, are given in the Supporting Information. In this section, we will just give a descriptive view of the projected solid.

In Figure 7a, we illustrate (in green) the centrally projected dodecahedron viewed down a fivefold axis. In the 120-cell, each of the pentagonal faces of this dodecahedron is capped by another dodecahedron.[5] As there are 12 pentagons in a given dodecahedron, the central dodecahedron is capped by 12 additional dodecahedra. These 12 additional dodecahedra are partially illustrated in Figure 7b (11 of the 12 dodecahedra are visible, and are illustrated in gray, cyan, and blue).

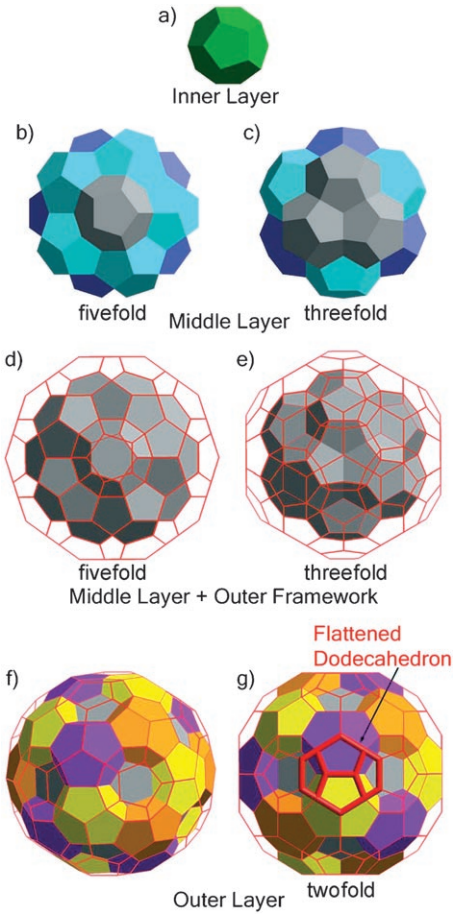

Figure 7. An I_h 3D projection of half of the 120-cell, a 4D polyhedroid. From center outward, a) a central dodecahedral cell (green), b) fivefold and c) threefold views of the 12 dodecahedral cells that are face-sharing to the central cell (gray, cyan, and blue), d) fivefold and e) threefold views outlining a layer of 32 dodecahedral cells that are face-sharing to the central 13 cells (red mesh), f) a view of the 32 cells with one cell type opaque (orange, yellow, and purple), and g) a twofold view of f) with one of the equatorial layer of 30 completely flattened dodecahedral cells highlighted in thick red cylinders.

There are numerous exposed pentagonal faces among the 11 visible dodecahedra of Figure 7b. In the 120-cell, there are capping dodecahedra on each of these pentagonal faces. To create this next shell of dodecahedra, we observe that there are two types of symmetry-inequivalent exposed pentagons in Figure 7b. Most exposed, and sitting directly above one of the pentagonal faces of the central dodecahedron, are 12 pentagons, all perfectly regular in appearance. One of these pentagons lies at the center of Figure 7b. We will place new exposed dodecahedra so that they perfectly cap these 12 regular pentagons.

There is, however, a second type of less exposed pentagonal face, which sits in the indentations of the illustrated cluster. These indented pentagonal faces appear in groups of three. One such grouping has been placed in the center of the view in Figure 7c. These threefold groupings of pentagonal faces provide the underside of a new set of dodecahedra. As there are 20 such indentations, there will be 20 new indented dodecahedra.

The vertices belonging to these two additional types of dodecahedra are shown in Figure 7d–e. For the sake of clarity, we have grouped these vertices as a spherical framework, while retaining the form of the 13 central dodecahedra as opaque polyhedra. In Figure 7d, we orient the figure along the fivefold axis. In the center of this figure, one of the new exposed dodecahedra can be seen. In Figure 7e, we rotate the perspective so that one of the indented dodecahedra lies at the center.

In Figure 7f, we illustrate these new dodecahedra by turning the indented dodecahedra into opaque objects (in yellow, orange, and purple, with no two adjacent indented dodecahedra being the same color). This figure illustrates not just the so-called indented dodecahedra, but, as indented dodecahedra share faces with the so-called exposed dodecahedra, the exposed dodecahedra as well. As this figure shows, both exposed and indented dodecahedra are significantly compressed after 3D projection (stereograms are given in the Supporting Information).

Even more interesting is yet a fourth view of the projected solid, Figure 7g. In this perspective, we rotate the polyhedron of Figure 7f so that four coplanar pentagons lie at the center of the picture. The appearance of these four pentagons should be directly compared with the four pentagons visible in the twofold view of an ordinary 3D dodecahedron, Figure 5d. Comparison shows that these four pentagons are identical in appearance. As we shall see, this identical appearance is not accidental. Rather, dodecahedra from the 4D 120-cell polyhedroid have become so compressed under projection into the 3D world that they have become absolutely flat, and have been reduced to being just four coplanar pentagons in appearance.

It turns out there are 30 of these absolutely flat dodecahedra, each lying directly above one of the bonds of the central dodecahedron. At this point we have described 75 dodecahedra: the one central one, its 12 nearest neighbors, the

[5] As mentioned previously, each face in a polyhedroid is always shared by two and only two polyhedra. This is analogous to the 3D case, in which each edge of a polyhedron is always shared by two and only two faces.

12 exposed dodecahedra, the 20 indented ones, and the 30 completely flat dodecahedra (75 = 1 + 12 + 12 + 20 + 30). As the name of the 120-cell implies, there are 45 remaining dodecahedra (45 = 120–75).

These remaining dodecahedra turn out to all lie in the shadow of the 75 other dodecahedra. Recall that cells in the shadow of other cells are polyhedra that, were they to be projected, would lie in the volumes already occupied by other polyhedra. The twofold 2D projection of the 3D dodecahedron is relevant here. In this earlier case, four of the 12 2D pentagonal faces are visible, four of the 2D faces have been reduced to 1D line segments, and four of the 2D faces lie in the shadow of the other faces.

Something very similar occurs in the projected 120-cell. Of the 120 3D dodecahedra, 45 of the dodecahedra project nicely (though are at times somewhat compressed) into 3D space, 30 of the dodecahedra project into 2D coplanar pentagons, and 45 of the dodecahedra lie in the shadow of the other dodecahedra.

Let us call a 4D sphere a spheroid. This spheroid can be divided into two equally sized hemispheroids. These hemispheroids, like the initial spheroid, are 4D in nature in just the same way that hemispheres, like spheres, are 3D. In our example, 45 dodecahedra lie in one hemispheroid and are projected into 3D space, 45 dodecahedra lie in the other hemispheroid (in the shadow of the first) and are not projected, and 30 dodecahedra lie between the two hemispheroids.

Recalling that the abutting points between the two 3D hemispheres of a sphere form a 2D circle, the equator, the points abutting these two 4D hemispheroids will also have a well-defined shape. Instead of an equatorial circle, this shape is an equatorial sphere. The centers of the 30 flat dodecahedra lie on this equatorial sphere.

This terminology helps us further understand the pictures in Figure 7d–g. In these pictures, the outermost vertices appear to lie on a sphere. This sphere is near the equatorial sphere to which the previous paragraph refers. This is important. In any 3D projection of a 4D polyhedroid, we need not consider any further cells once we reach the equatorial sphere; all further cells will lie in the shadow of the other cells, and cells which lie on the equatorial sphere are readily identified because they are always flat.

The 600-cell: We now turn to the 600-cell, the 4D Platonic solid with the greatest number of cells, and the polyhedroid that is most relevant to the current paper. 600 is a daunting number. Fortunately, there is a simple relation between the 600-cell and the 120-cell: the two are duals of each other. The 600-cell and the 120-cell therefore lie in the same relation to one another as do the icosahedron and dodecahedron. In 3D, two polyhedra are duals of each other if the points at the centers of the faces of one polyhedron lie at the vertices of the other polyhedron.

Something analogous will happen for dual polyhedroids: the points at the centers of the cells of one polyhedroid lie at the vertices of the other polyhedroid. Thus, the dual of the 120-cell has a vertex at the center of each of the 120 cells of the 120-cell. The dual of the 120-cell has exactly 120 vertices.

As each cell of the 120-cell has 12 neighboring cells (see previous section), each vertex in the dual of the 120-cell will have 12 neighboring vertices. These vertices respect the original I_h symmetry of the dodecahedron, and form a perfect icosahedron around the central vertex. Consider any one of the 20 triangular faces of this icosahedron. Each of these faces, together with the center of the icosahedron, forms a tetrahedron (in 3D this tetrahedron is not perfectly regular, but in 4D it can be perfectly regular). Thus, if each vertex of the dual of the 120-cell has an icosahedron of vertices around it, each vertex is shared by 20 tetrahedra.

The following equation holds: (number of vertices) × (number of tetrahedra which share a common vertex)/(number of vertices per tetrahedron) = (number of cells). For the dual of the 120-cell, there are 120 vertices, 20 tetrahedra which share a common vertex, and 4 vertices per tetrahedron. Therefore, the dual of the 120-cell has exactly 600 cells (600 = 120 × 20/4). These cells are all tetrahedra.

Projected 600-cell: We now construct a 3D projection of the 600-cell. We choose the canonical direction for projection, that is, the one orthogonal to the 3D space defined by one of the cells of the 600-cell.[6] As projected images preserve the symmetry of the projected cell and as the cells of the 600-cell are tetrahedra, this 3D projection will be of T_d symmetry. Its central tetrahedron is shown in Figure 8a. Following standard intermetallic nomenclature, this central tetrahedron is called the inner tetrahedron (IT).

For all polyhedroids, every face is shared by exactly two polyhedra. In the 600-cell, every triangular face is therefore shared by two tetrahedra. Each face of the central tetrahedron in Figure 8a is therefore the face of a second tetrahedron. By placing capping vertices on each face, we generate the four required additional tetrahedra. As Figure 8b shows, these four capping vertices themselves lie at the corners of a larger outer tetrahedron, OT. The polyhedron formed from both the IT and OT sites is referred to as a stella quadrangula, and is shown in Figure 8c.

The exposed triangular faces of the stella quadrangula are all symmetry-equivalent, and form pairs of edge-sharing faces. These faces lie in an indented orientation with respect to each other. Three such pairs of indented faces are shown in Figure 8c. By $\bar{4}$ symmetry, there are three further pairs of

[6] There is another relevant direction for projecting the 600-cell. In this alternate projection, the center of projection is the volume directly surrounding one of the 120 vertices of the 600-cell. Under such a projection, the 600-cell projects into an I_h 3D object. This 3D object consists of a central vertex, surrounded by the 12 vertices of an icosahedron, followed by the 20 vertices of a dodecahedron, followed by 12 vertices of a larger icosahedron. Finally come 30 vertices of an icosidodecahedron. This icosidodecahedron lies on the equatorial sphere. This collection of polyhedra is related to the Bergman cluster of quasicrystalline fame.[1] This alternate projection is deeply relevant to intermetallic crystal structures, but structures of a type different from the ones discussed in the current article; see the Supporting Information.

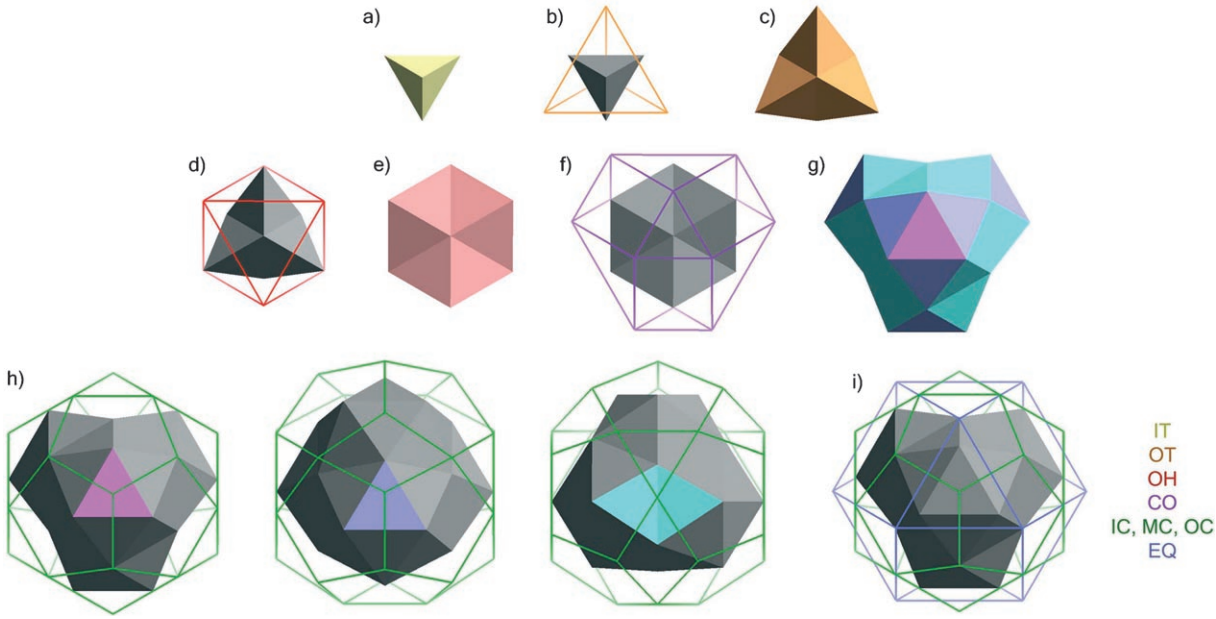

Figure 8. A T_d 3D projection of half of the 600-cell, a 4D polyhedroid. a) A central tetrahedral cell consisting of four IT vertices (yellow), b) four OT vertices capping its faces, c) the new triangular faces formed by the capping with OT (orange), d) six OH vertices capping these faces (red), e) the new triangular faces formed by the capping with OH (pink), f) 12 CO vertices capping these faces (purple), g) the three distinct triangular faces formed by the capping with CO (magenta, blue and cyan), h) 28 OC, MC, and IC vertices capping these faces (green framework), and i) 12 EQ vertices on the equator of the 600-cell (blue framework).

indented faces that lie on the underside of the figure. We place six capping vertices, one above each pair of indented faces. The six new vertices are shown in Figure 8d. As this figure shows, the new vertices lie in an octahedron and are therefore called the octahedral sites, OH.

The exposed triangular faces of the IT-OT-OH cluster (Figure 8e) are all symmetry-equivalent, and again can be viewed as being composed of indented edge-sharing faces. Trios of these edge-sharing faces come together in the form of corrugated rosettes; one such rosette is at the center of Figure 8e. Above each pair of indented edge-sharing faces we place a new capping vertex. As there are three such indented edge-sharing faces per rosette, and four rosettes in total, there are 12 new capping vertices. These capping vertices form a distorted cuboctahedron (Figure 8f), the CO sites. The capped cluster composed of the IT-OT-OH-CO sites is an edge-capped stella quadrangula. A view of the edge-capped stella quadrangula is given in Figure 8g.

However, the construction is not yet finished; there are three different kinds of exposed triangular faces in the edge-capped stella quadrangula. These faces are illustrated in Figure 8g. The most exposed of the three types of faces is shown in magenta. Slightly less exposed are faces, edge-sharing to the most exposed faces, shown in blue. Finally, there are pairs of indented edge-sharing faces, shown in cyan.

We cap the most exposed faces, the less exposed faces, and the pairs of indented faces with new vertices. As there are four most exposed faces, 12 less exposed faces, and 12 pairs of indented faces, we place 28 (28=4+12+12) new vertices onto our cluster. These 28 vertices are drawn as a shell in Figure 8h. In this figure, we show the 28-vertex shell and the edge-capped stella quadrangula from three different perspectives: down the most exposed face (left), less exposed face (middle), and indented faces (right). Atoms capping respectively the most exposed, less exposed, and indented faces are termed OC (for outer capping), MC (for middle capping), and IC (for inner or indented capping). The capping atoms together with the faces beneath the capping vertices form new tetrahedra. These new tetrahedra are quite compressed. This compression is particularly clear in the stereograms given in the Supporting Information.

We now come to the last site of the projected 600-cell. This site proves to lie exactly on the equatorial sphere of the 600-cell (for this reason, this site will be called EQ). The EQ site is most easily seen by recalling that every vertex in the 600-cell lies in the center of an icosahedron, and that every vertex of an icosahedron has five neighboring vertices which lie in a pentagon around it.

Examination of Figure 8h shows that the outer shell of 28 atoms has 12 pentagonal faces. Near the center of these faces, but just below the plane of these faces, lies a CO atom. We can now envision that this CO atom, together with the pentagon of atoms above it, forms the underside of an extraordinarily compressed icosahedron. We place the EQ atoms at the center of this compressed icosahedron. These EQ positions are shown in Figure 8i.

Beyond this point, projected vertices lie in the shadow of the other points and need not be further considered. In summary, the interior of the projected 600-cell consists of 54 vertices (4IT+4OT+6OH+12CO+12IC+12MC+4OC=

54). On the equatorial sphere lie an additional 12 vertices (EQ). A further 54 sites lie in the shadow of the above sites, and are not included in the 3D projection (by symmetry, the number of shadowed sites exactly equals the number of sites in the interior of the 3D projection). As $120=54+12+54$, we have accounted for all 120 vertices of the 600-cell.

Of the sites discussed, the first 54 of these 120 vertices will prove most important for the remainder of this paper. For the sake of convenience, we term the cluster formed by these 54 vertices the 54-cluster.

The $F\bar{4}3m$ structures: In the previous section of this paper, we have seen that the 4D Platonic solid composed of stuffed icosahedra, the 600-cell, can be projected into a 3D space as a cluster with 54 interior and 12 equatorial vertices. These interior sites bear the names IT, OT, OH, CO, IC, MC, and OC. Earlier in the paper, we saw that the atoms of $F\bar{4}3m$ structures can be specified by three-letter designations, the first letter specifying the cluster origin and the final two letters the cluster site (CC, IT, OT, OH, TT, or CO). Most importantly, we see that four of the letter designations of the projected 600-cell are the same as those for $F\bar{4}3m$ cluster types: IT, OT, OH, and CO. This is not a duplication of symbols: there is a real connection.

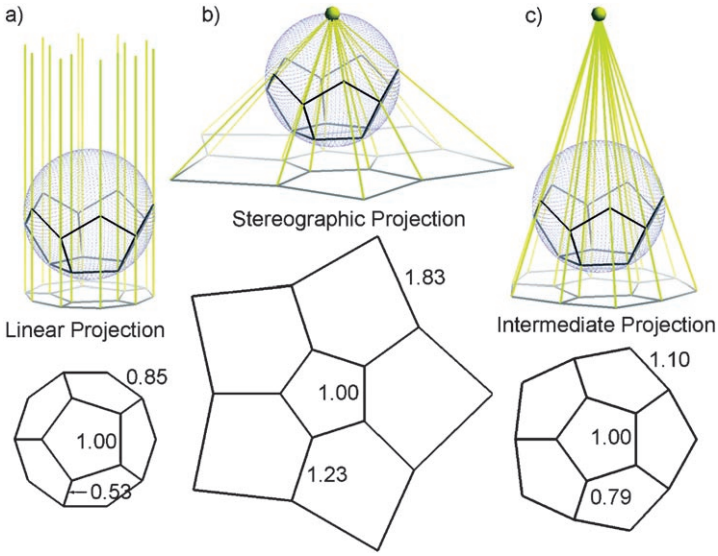

Figure 9. Schematic views of the three types of projection relevant to this paper: a) linear projection, b) stereographic projection, and c) intermediate projection. While bonds become unphysically short toward the outside of a linear projection and unphysically long toward the outside of a stereographic projection, bonds can retain reasonably constant lengths for a hemisphere with intermediate projection.

Linear, stereographic, and intermediate projection: To explore the tie between the 4D 600-cell polyhedroid and our cubic structures, we need a way to exactly specify the 3D location of a given vertex of the projected 600-cell. To do so, we need to carefully examine what we mean by projection. The projections we are interested in will always be projections from 4D space to 3D space. However, as we know from cartography, there are numerous ways of projecting a sphere onto a plane: no one of these projections is inherently better than all others. The same will prove true in projecting the 4D spheroids into 3D space.

Scientists are most familiar with two different types of projection.[7] First, they are familiar with linear projection (see Appendix), but many of us are also familiar with a second type of projection, stereographic projection.[49] In Figure 9a,b, we give schematic views of both linear and stereographic projection. As we are most familiar with 2D maps based on the 3D globe, these schematics illustrate projection of 3D space to 2D space. As we shall see, these same ideas can be applied to projecting 4D space to 3D space.

As Figure 9a shows, we can imagine the hemisphere of a Platonic solid (in this figure, a dodecahedron) to lie on the surface of a transparent sphere. We place a light source sufficiently far away from this sphere that rays emanating from this light source are essentially parallel to one another. In linear projection, we place a plane normal to these rays of light on the opposite side of the sphere and locate the shadow of the Platonic solid.

[7] Other types of projection, of course, exist. In the problem of mapping the 600-cell from 4D to 3D, various techniques have been used, often requiring the introduction of disclinations.[47,48]

In stereographic projection, we again consider a single light source, but this time place it directly on the surface of the sphere (at the point opposite the projected plane), Figure 9b. In stereographic projection, unlike linear projection, no vertices, bonds, or faces lie in the shadow of other vertices, bonds, or faces; however, on a simple level, we tend to view stereographic projection as more distorted than linear projection.

On the plus side, both linear and stereographic projection preserve the fivefold axis directly opposite the light source. In the examples of Figure 9a,b, the point directly opposite the light source has fivefold symmetry and both the linear and stereographic projected images retain fivefold symmetry.

Bond lengths, however, prove an issue. These problems can be understood with just one look at Figure 9a,b. In stereographic projection, bond lengths can become unreasonably large toward the outside of the projected image. But linear projection also has issues, as bonds can become unreasonably short toward the outside of the projection. Bonds exactly parallel to the direction of projection have their lengths collapse to zero.

As neither stereographic nor linear projection is suitable for preserving bond lengths, and as uniform bond lengths are something chemists would like to see in any representation, we will need to consider new forms of projection. We wish to choose a method of projection that retains the ability to preserve the symmetry of the central point of the projection, and which does a superior job in preserving bond lengths.

This new method of projection must be equally suited to 3D projection onto a 2D plane, as well as 4D projection into

3D space. In both cases, we wish to preserve the symmetry at the center of the projection (for the former at the center of a 2D polygon, and for the latter at the center of a 3D polyhedron), while at the same time keeping variation in bond lengths (for the former for bonds in the 2D plane, and for the latter for bonds in 3D space) to a minimum.

The chemical entities studied in this paper are based on the 54-cluster of the projected 600-cell. We will therefore choose a projection that preserves the T_d symmetry of the 54-cluster, and which does a reasonable job in keeping bond lengths constant.

Our proposed projection is a simple one. We place the light source at a point intermediate between the location for stereographic projection (where it lies on the sphere or spheroid) and linear projection (where it lies infinitely far away), Figure 9c. As bond lengths become too long in stereographic projection and too short in linear projection, we thus achieve a happy medium. (The distances can never all be equal, but one can aim for maximum similarity.)

Least squares optimization of bond lengths shows that for the 54-cluster (a 4D to 3D projection), a light source 1.9 spheroid diameters away from the center of the projection preserves distances best (see Appendix). In Table 2, we compare a variety of bond lengths for linear, stereographic, and this alternate projection. (The choice of the ten distances given in Table 2 is not a random one: as we shall later discuss, these ten bond lengths may be used to derive the ten site parameters on which the 54-cluster is based.) As this table shows, bond lengths are much more constant with the new method. We call this projection method intermediate projection. The formulas and sites corresponding to the 54-cluster are given in the Appendix to this paper.

Table 2. Comparison of projected 54-clusters. The IT–IT distance of $2\sqrt{2}$ is arbitrarily chosen. It does, however, correspond roughly to bond lengths of the $F\bar{4}3m$ structures.

Bond	Linear [Å]	Stereographic [Å]	Intermediate [Å]
IT–IT	2.828	2.828	2.828
OT–IT	2.763	2.933	2.847
OH–IT	2.649	3.004	2.820
CO–IT	2.322	3.135	2.692
CO–OT	2.649	3.251	2.915
IC–OT	2.000	3.501	2.610
IC–CO	2.649	3.736	3.094
MC–OH	1.732	3.773	2.496
MC–CO	2.322	3.929	2.921
OC–CO	2.000	4.070	2.709
mean	2.391	3.416	2.793
std. dev.	0.377	0.445	0.172

$F\bar{4}3m$ structures and 54-clusters: With this choice of projection in hand, we are ready to establish the connection between the common atoms of the $F\bar{4}3m$ crystal structures and the 54-cluster derived from the 600-cell. First, let us get our bearings in the $F\bar{4}3m$ structures. As we have mentioned previously, this paper considers only those $F\bar{4}3m$ structures which contain a γ-brass cluster. For ease of comparison, we convert the coordinates of the reported crystal structures so that these γ-brass clusters are centered at the origin.[8] These converted coordinates are given in the Supporting Information.

The γ-brass cluster consists of IT, OT, OH, and CO atoms, and by placing this cluster at the origin, these sites are labeled ZIT, ZOT, ZOH, and ZCO. (Recall that Z, Q, H, and T refer to clusters centered at zero, a quarter, a half, and three-quarters along the cell dimension: the Z in these labels therefore specifies a cluster centered at the origin.) We now examine the atoms that lie just outside this cluster. We turn first to the $Li_{21}Si_5$ structure. As Figure 10 shows, surrounding the γ-brass core are three additional Li sites: QCO, TCO, and TOT sites.

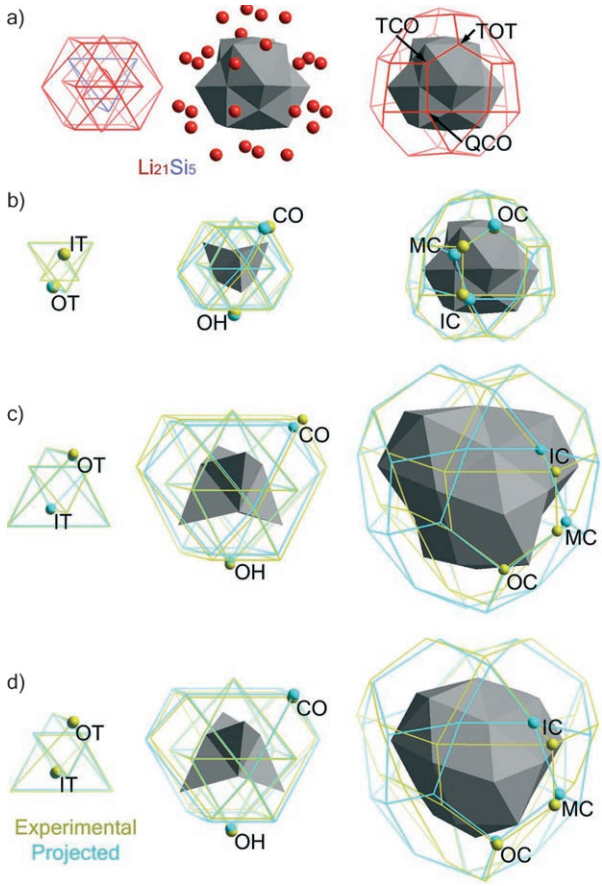

Figure 10. A 54-cluster in $Li_{21}Si_5$ where nearest neighbors are bonded to one another, shown a) by atom type (Li: red, Si: blue) and b) comparison of a) with an intermediate projection of the 54-cluster (experimental sites in yellow, projected in cyan). Larger 54-clusters in c) $Mg_{44}Rh_7$ and d) $Li_{21}Si_5$, also compared to intermediate projections.

[8] In the $F\bar{4}3m$ space group, the Z, Q, H, and T sites are the 4a, 4b, 4c, and 4d special sites all with equal T_d symmetry. It is therefore possible to translate the unit cell so that a γ-brass cluster centered at any of these positions is shifted to lie at the origin. In making such a translation, we must also pay attention to the orientation of the γ-brass cluster. As the γ-brass cluster is non-centrosymmetric, there are two possible orientations. The IT atom is located at (x,x,x); we have chosen this atom to always lie near (.95,.95,.95), rather than (.05,.05,.05).

In Figure 10a (right), we draw the shell formed by the three additional sites. This shell has 28 atoms in it. We recall that the 54-cluster also contains 28 atoms placed in a shell around a 26 atom core. In Figure 10b, we directly compare the 54 atoms based on atoms at ZIT, ZOT, ZOH, ZCO, QCO, TCO, and TOT (shown in yellow) with the intermediate projected 54-cluster (shown in cyan). As this figure shows, the projected 54-cluster has vertices near the actual atomic sites of $Li_{21}Si_5$. The seven aforementioned sites therefore correspond to respectively the seven sites of the 54-cluster: IT, OT, OH, CO, IC, MC, and OC.

In Table 3, we list the atomic positions for the eight $F\bar{4}3m$ structure types.[9] As this table shows, the eight structure types contain common sites at the seven aforementioned positions. All $F\bar{4}3m$ structures therefore contain a 54-cluster centered at the origin. But Table 3 also reveals additional sites common to all members of the $F\bar{4}3m$ family of structures. Can these additional common sites also be traced to 54-clusters?

Table 3. Atomic sites of $F\bar{4}3m$ structures. Sites common to all structure types are given in italics. See text for discussion of *HOH* and *HTT*. $Li_{21}Si_5$: $Li_{21}Si_5$, $Zn_{21}Pt_5$, and $Cu_{41}Sn_{11}$; $Mg_{44}Rh_7$: $Mg_{44}Rh_7$, $Zn_{39}Fe_{11}$, and $Mg_{44}Ir_7$; $Zn_{13}(Fe, Ni)_2$; Mg_6Pd: Mg_6Pd and $Mg_{29}Ir_4$; Na_6Tl; $Zn_{91}Ir_{11}$; $Li_{13}Na_{29}Ba_{19}$; $Al_{69}Ta_{39}$. Reference [35] reports a second HTT site in $Li_{13}Na_{29}Ba_{19}$.

$Li_{21}Si_5$	$Mg_{44}Rh_7$	$Zn_{13}(Fe,Ni)_2$	Mg_6Pd	Na_6Tl	$Zn_{91}Ir_{11}$	$Li_{13}Na_{29}Ba_{19}$	$Al_{69}Ta_{39}$
ZIT	*ZIT*	*ZIT*	*ZIT*	*ZIT*	*ZIT*	*ZIT*	*ZIT*
ZOT	*ZOT*	*ZOT*	*ZOT*	*ZOT*	*ZOT*	*ZOT*	*ZOT*
ZOH	*ZOH*	*ZOH*	*ZOH*	*ZOH*	*ZOH*	*ZOH*	*ZOH*
ZCO	*ZCO*	*ZCO*	*ZCO*	*ZCO*	*ZCO*	*ZCO*	*ZCO*
–	–	–	–	–	–	QCC	QCC
QIT	–	–	–	–	–	–	–
QOT	*QOT*	*QOT*	*QOT*	*QOT*	*QOT*	*QOT*	*QOT*
QOH	QOH	QOH	QOH	QOH	QOH	–	–
QCO	*QCO*	*QCO*	*QCO*	*QCO*	*QCO*	*QCO*	*QCO*
–	–	–	–	–	–	QTT	QTT
–	–	HCC	HCC	HCC	HCC	HCC	HCC
HIT	–	–	–	–	HIT	–	–
HOT	*HOT*	*HOT*	*HOT*	*HOT*	*HOT*	*HOT*	*HOT*
HOH	*HTT*	*HTT*	*HTT*	*HTT*	*HTT*	*HTT*	*HTT*
HCO	*HCO*	*HCO*	*HCO*	*HCO*	*HCO*	*HCO*	*HCO*
–	–	–	–	–	HOH	HTT	–
–	–	TCC	–	–	–	–	TCC
TIT	TIT	TIT	–	TIT	TIT	TIT	TIT
TOT	*TOT*	*TOT*	*TOT*	*TOT*	*TOT*	*TOT*	*TOT*
TOH	*TOH*	*TOH*	*TOH*	*TOH*	*TOH*	*TOH*	*TOH*
TCO	*TCO*	*TCO*	*TCO*	*TCO*	*TCO*	*TCO*	*TCO*

Let us turn to clusters that might be centered at Q. An examination of Table 3 shows that only one of the eight structure types has a QIT atom. As an IT atom is an essential ingredient of any 54-cluster, at first glance we might conclude that there could be no common 54-cluster centered at Q, but we would be wrong.

The absence of QIT atoms does not imply the absence of a 54-cluster; rather it means that if there is a 54-cluster centered at Q, its length scale must be different from the length scale of the common 54-cluster centered at Z. If we are to examine Q-centered clusters, we must consider larger distances. We have not far to look. All eight structure types contain a QOT site. These QOT atoms also lie in a tetrahedron. The QOT atoms are separated from each other by distances of approximately the golden mean ($\tau = (1+\sqrt{5})/2$) times a typical metal bond length.

We now proceed to search for the remaining six sites of a 54-cluster. We recall that each of these six sites successively caps triangular faces formed by more central atoms. In Figure 10c, we show the cluster formed from the QOT, TOT, TOH, HTT, TOT, TCO, and HOT sites of the $Mg_{44}Rh_7$ system. We compare the cluster formed from these sites with the sites of the intermediate projected 54-cluster. As this figure shows, there is fair agreement between the crystal coordinates and the mathematically constructed 54-cluster.[10] The aforementioned sites therefore can be thought to correspond to the IT, OT, OH, CO, IC, MC, and OC sites of a 54-cluster the nearest-neighbor distances of which are approximately τ times a standard metal bond length.

Table 3 shows that seven of the eight structure types have the above-mentioned suite of atoms. However, the $Li_{21}Si_5$ structure, instead of containing the HTT site, has an HOH site. In Figure 10d, we show the cluster generated from the same set of atoms, but in which the HTT site has been replaced with the HOH site. As this figure shows, this replacement in no way alters the presence of a 54-cluster.

The 54-clusters centered at Q are quite large with respect to the primitive unit cell. They are sufficiently large that the HOH atom in the $Li_{21}Si_5$ structure can provide the IC site

[9] For this article, we use Table 3 to define structure types. We assume two compounds which have the same atomic sites in Table 3 belong to the same structure type. Thus, elemental ordering over the sites is not taken into account. Actual elemental ordering is given, however, in the tables in the Supporting Information.

[10] Agreement is fair with the exception of the IC site. This is a general trend. The IC site is typically the site with the greatest disparity between mathematically constructed and experimentally observed positions. Recall that the IC site has highly compressed tetrahedra around it, and that as it caps two different triangular faces of the edge-capped stella quadrangula beneath it, the atomic site cannot readily move to decompress these tetrahedra. For these reasons, the tetrahedra around the IC atoms are the least regular in appearance and therefore, we suspect, the least ideal.

for two neighboring 54-clusters. By contrast, in the $Zn_{91}Ir_{11}$ system the HTT atoms are not shared by neighboring clusters. The former systems therefore require half the number of IC atoms that the latter systems require. There are six HOH atoms in an octahedron versus 12 HTT atoms in a truncated tetrahedron. This change from an HTT site to an HOH site is therefore exactly what is required if two clusters are to share the same IC site.

As the HOH and HTT sites serve the same function, we consider for the sake of this paper that they are a common atomic site. We have used this viewpoint in both Tables 1 and 3. We see that there is a common Q-centered 54-cluster throughout the $F\bar{4}3m$ family. In exactly the same manner, we can search for other 54-clusters. There are many to be found, an average of 4.5 clusters per structure type, the full list of which are given in Table 4. (In Table 4, we portray the eight structure types with just six groupings, because two pairs of structure types, Mg_6Pd and $Zn_{13}(Fe,Ni)_2$, as well as Na_6Tl and $Zn_{91}Ir_{11}$, have the exact same list of 54-clusters.)

Table 4, in addition to showing the atomic sites of a given 54-cluster, also attempts to give some measure of the average distances found in each cluster. As each cluster has many nearest-neighbor distances, and as the atomic sites at which the atoms lie are at high-symmetry points, some thought is called for in the calculation of average distances.

In this paper, we consider the following: IT, OT, and OC atoms lie at (x,x,x) special positions; OH atoms lie at $(x,0,0)$; and finally, CO, IC, and MC atoms lie (with the above-mentioned exception of the HOH site) at (x,x,z) positions. Therefore, one geometric parameter defines the IT, OT, OH, and OC positions, while two parameters define the CO, IC, and MC distances. There are a total of ten parameters needed to define the size and shape of a 54-cluster.

We can therefore define any 54-cluster with the appropriate choice of ten nearest-neighbor distances. We choose these canonical distances by considering links between a given atom and atoms more centrally located in the cluster. The ten distances chosen are IT–IT, OT–IT, OH–IT, CO–IT, CO–OT, IC–OT, IC–CO, MC–OH, MC–CO, and OC–CO. In this list, the IT–IT distance defines the single parameter of the IT position, the OT–IT bond defines the single parameter of the OT position, and so forth.

We may directly calculate these ten canonical distances from knowledge of the ten atomic site parameters. Conversely, the ten atomic site parameters can be specified from the ten canonical distances. While atomic site parameters are the most typical way to represent atomic positions, the canonical distances are nonetheless of interest. In intermediate projection, bond lengths are fairly constant across all bonds in the 54-cluster. When the canonical bond lengths are close to each other in value, the atoms will therefore prove to lie particularly near the positions of an intermediate projected 54-cluster.

In the Supporting Information, we present canonical nearest-neighbor distances for all 54-clusters found in the $F\bar{4}3m$ structures. In Table 4, we present a summary of this data. In particular, we show the ratio of the *a*-axis cell length divided by the average of the ten canonical distances. With this value, we also show the standard deviation among the ten canonical bond lengths. As Table 4 shows, for all but one of the myriad of 54-clusters, calculated ratios are in the range of either 6.4–6.8 or 3.4–3.9. The former range corresponds to nearest-neighbor distances at ordinary bond lengths, the latter to the golden mean times that number.

Table 4 also shows that for the former range, the standard deviation of bond lengths centers around the value of 0.2 Å. This value can be directly compared to the ideal mathematical variation of 0.17 Å (associated with the intermediate projection method) shown in Table 2. The actual variation in bond lengths is not much greater than that which is mathematically obtainable. For 54-clusters in the 3.4–3.9 range, the variation in cluster distances is greater, with the smallest standard deviations near 0.6 Å in value. This more than doubling in standard deviations is partially accounted for by the increase of the actual cluster distances. However, note that as there is an average of 4.5 54-clusters per structure type, but only twenty or so atomic parameters per structure type, uniformly small standard deviations across all cluster sizes are difficult to achieve.

Table 4. 54-Clusters in $F\bar{4}3m$ structures. Atoms common to all structure types are in italics (see also Table 3). Unlike $Li_{21}Si_5$, in $Cu_{41}Sn_{11}$ the smaller H cluster is not inverted with respect to the other clusters. Therefore, IT and OT should be HIT and *HOT*, respectively.

	a/d[a]	σ[b] [Å]	IT	OT	OH	CO	IC	MC	OC
$Li_{21}Si_5$; $Zn_{21}Pt_5$; $Cu_{41}Sn_{11}$									
Z	6.62	0.12	*ZIT*	*ZOT*	*ZOH*	*ZCO*	*QCO*	*TCO*	*TOT*
Q	6.62	0.20	QIT	*QOT*	QOH	*QCO*	*HCO*	*ZCO*	*ZOT*
H	6.42	0.37	*HOT*	HIT	*HOH*	*HCO*	*QCO*	*TCO*	TIT
T	6.64	0.15	TIT	*TOT*	*TOH*	*TCO*	*ZCO*	*HCO*	*HOT*
Z	3.70	0.38	*ZOT*	*TOT*	*HOH*	QOH	*HOT*	*HCO*	*QOT*
Q	3.81	0.29	*QOT*	*ZOT*	*TOH*	*HOH*	*TOT*	*TCO*	*HOT*
H	3.62	0.55	HIT	TIT	*ZOH*	QOH	*ZCO*	*ZCO*	QIT
T	3.70	0.38	*TOT*	*HOT*	QOH	*ZOH*	*QOT*	*QCO*	*ZOT*
$Mg_{44}Rh_7$; $Zn_{39}Fe_{11}$; $Mg_{44}Ir_7$									
Z	6.68	0.18	*ZIT*	*ZOT*	*ZOH*	*ZCO*	*QCO*	*TCO*	*TOT*
T	6.78	0.20	TIT	*TOT*	*TOH*	*TCO*	*ZCO*	*HCO*	*HOT*
Q	3.78	0.57	*QOT*	*ZOT*	*TOH*	*HTT*	*TOT*	*TCO*	*HOT*
T	3.77	0.65	*TOT*	*HOT*	QOH	*ZOH*	*QOT*	*QCO*	*ZOT*
$Zn_{13}(Fe,Ni)_2$; Mg_6Pd; $Mg_{29}Ir_4$									
Z	6.75	0.15	*ZIT*	*ZOT*	*ZOH*	*ZCO*	*QCO*	*TCO*	*TOT*
Q	3.49	0.96	*QOT*	*ZOT*	*TOH*	*HTT*	*TOT*	*TCO*	*HOT*
T	3.67	0.69	*TOT*	*HOT*	QOH	*ZOH*	*QOT*	*QCO*	*ZOT*
Na_6Tl; $Zn_{91}Ir_{11}$									
Z	6.71	0.16	*ZIT*	*ZOT*	*ZOH*	*ZCO*	*QCO*	*TCO*	*TOT*
T	6.82	0.14	TIT	*TOT*	*TOH*	*TCO*	*ZCO*	*HCO*	*HOT*
Q	3.63	0.65	*QOT*	*ZOT*	*TOH*	*HTT*	*TOT*	*TCO*	*HOT*
H	3.79	0.42	*HOT*	*QOT*	*ZOH*	*TOH*	*ZOT*	*ZCO*	*TOT*
T	3.77	0.72	*TOT*	*HOT*	QOH	*ZOH*	*HTT*	*QCO*	*ZOT*
$Li_{13}Na_{29}Ba_{19}$									
Z	6.77	0.34	*ZIT*	*ZOT*	*ZOH*	*ZCO*	*QCO*	*TCO*	*TOT*
T	7.77	0.45	TIT	*TOT*	*TOH*	*TCO*	*ZCO*	*HCO*	*HOT*
Q	3.51	0.92	*QOT*	*ZOT*	*TOH*	*HTT*	*TOT*	*TCO*	*HOT*
H	3.83	0.76	*HOT*	*QOT*	*ZOH*	*TOH*	*ZOT*	*ZCO*	*TOT*
$Al_{69}Ta_{39}$									
Z	6.75	0.14	*ZIT*	*ZOT*	*ZOH*	*ZCO*	*QCO*	*TCO*	*TOT*
Q	3.42	0.95	*QOT*	*ZOT*	*TOH*	*HTT*	*TOT*	*TCO*	*HOT*
H	3.62	0.66	*HOT*	*QOT*	*ZOH*	*HCO*	QTT	*ZCO*	*TOT*

[a] d = average distance. [b] σ = standard deviation.

We present this same data graphically in Figure 11. In this figure, we plot the ratio of (cell axis length)/(average nearest-neighbor distance), together with its corresponding standard deviation for all clusters of all 13 structures belonging to the eight structure types. This figure shows clearly the

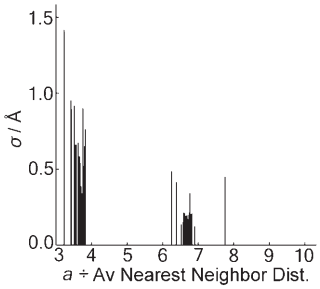

Figure 11. The standard deviation versus mean nearest-neighbor distance in each experimental occurrence of the 54-cluster among the $F\bar{4}3m$ structures. Data is based on Table S2 of the Supporting Information.

two apparent size ratios: *a*/(average distance) gives values of either approximately 4 or 6. One of the primary goals for the remainder of this paper will be to account for these most common size ratios.

Diffraction of a single 54-cluster: We have seen there is a relation between the atomic sites in the $F\bar{4}3m$ structures and the 3D projected image of the 4D 600-cell. We now examine how the fivefold symmetry operations of the 4D 600-cell are retained as pseudo-symmetries in its 3D projection.

There are an enormous number of fivefold symmetries in the full 4D 600-cell. If we recall that every pair of adjacent vertices (i.e., every bond) of the 600-cell is bisected by a pentagonal face of the dual 120-cell, and that each of these pentagonal faces has fivefold symmetry, we recognize that every bond in the 600-cell defines a set of fivefold symmetry operations. Before projection, all bonds have exact fivefold symmetry.

After 3D projection, different bonds differ in the extent to which they retain their fivefold symmetry. The bonds nearest the center of projection retain the most of the original fivefold symmetry. (Recall that the symmetry of the exact center of the projection is perfectly preserved, and that the further one travels from this center, the more imperfect the resultant images usually become.) In the 3D projection discussed in this paper, we have chosen the center of the projection to be the center of one of the tetrahedral cells of the 600-cell. There are six fivefold axes that lie nearest this center: the six edges of the central tetrahedron. The fivefold symmetry is best preserved for these six axes.

In Figure 12a, we redraw the 54-cluster so that one of the six edges of its central tetrahedron is placed at the center of the image. In Figure 12b, we consider this exact same orientation, but keep only the bonds that appear as pentagons or decagons in the projected image. It may be seen that 50 of the 54 atoms lie either at the center of this view or on a pentagon or decagon.

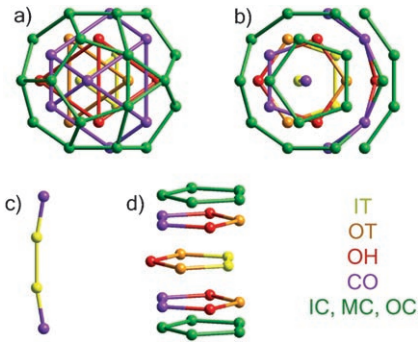

Figure 12. Features of pseudo-fivefold symmetry in the linear projection of a 54-cluster. a) A view of the 54-cluster along one of the bonds of its central tetrahedron, b) the pentagons and the decagon within this unit, and a perpendicular view of c) the four core atoms, and d) five pentagons. From the center outward, sites are shown in yellow, orange, red, purple, and green. See Figure 8 for site names.

In Figure 12c,d, we show the perpendicular view of the core atoms, and the individual pentagons. It may be seen that there are four core atoms (Figure 12c) and five different pentagons (Figure 12d). The structure of the so-called decagon is more complex and is not shown in this figure. It consists of 21 atoms with an approximate fivefold symmetry.[11]

Plane waves and the 54-cluster: We now turn to the diffraction image of the 54-cluster. As yet, we have not placed the cluster into a crystalline unit cell. Even so, we can generate relevant images. Consider the Fourier transform of the 54-cluster.[12]

Note that the constant scattering factor for each atom is taken to be unity.[13] To apply this Fourier transform, we need to explicitly determine the 54 $\vec{r}_j$ coordinates. We consider

[11] The so-called decagon could be viewed as five pentagons with four defect sites, but we need not enter the full complexity of the decagon, as our primary interest is the pseudo-tenfold diffraction symmetry normal to the [110] direction. As readers familiar with diffraction theory know, in such cases we need only consider the 2D projection of atoms normal to the desired direction to calculate exact structure factors.[50] Figure 12b gives an adequate view of this 2D projected structure.

[12] For those accustomed to seeing X-ray diffraction patterns, the use of Fourier transforms here may seem unorthodox. The Fourier transforms used in this paper resemble more closely the Fourier transforms used to study clusters in the gas phase, and can be seen as the analogue of diffraction patterns without the constraints of a unit cell. As in a diffraction pattern, the $\vec{k}$ vector corresponds to the direction and frequency of plane waves running through the cluster, and the contours to the degree to which atoms constructively interfere with the waves.

[13] By taking the scattering factor of each atom to be unity, we do not treat the coloring problem in this paper. We cannot expect the type of 4D to 3D projection in this paper to hold the key to the coloring problem, as evidenced by the different atomic site preferences in the small and large 54-clusters throughout this family of structure types. While the large clusters tend to consist mainly of larger and/or more electronegative atoms, the small clusters have no evident occupancy pattern. Still, we expect that the answer to the coloring problem is closely related to this projection method, and we plan to explore this point in our subsequent work.

both a linear and an intermediate projected 54-cluster. Looking ahead to the actual crystal structure, we define an IT–IT bond to run in the $[1\bar{1}0]$ direction. We further consider only those $\vec{k}$ that are orthogonal to this direction. With these givens, we can calculate the magnitude of $F_{\vec{k}}$ as a function of $\vec{k}$ [Eq. (1)]. This is plotted in Figure 13. (Figure 13a,b are the diffraction images of linear and intermediate projected 54-clusters, respectively.)

$$F_{\vec{k}} = \sum_{j=1}^{54} e^{2\pi i \vec{k}\cdot\vec{r}_j} \qquad (1)$$

As this figure shows, there are a few particularly large peaks in the Fourier transform. Especially towards the center of this diffraction image, these peaks appear in rings of ten. Three such possible rings are shown in Figure 13. In the innermost ring, labeled 4, all 10 reflections are clearly visible. For the 6-ring, six of the ten peaks are clear for both the linear and the intermediate projected 54-clusters. The remaining four additional peaks can also be discerned in the intermediate projected 54-cluster diffraction pattern. For the 10-ring of the linear projected 54-cluster, only the reflections along the horizontal axis (the $[k_1k_1 0]$ direction) are present. By contrast, for the intermediate projected 54-cluster, the 10-ring reveals an additional set of four peaks. All of the above peaks lie at similar orientations along the concentric rings, orientations which correspond to a pseudo-tenfold diffraction symmetry.

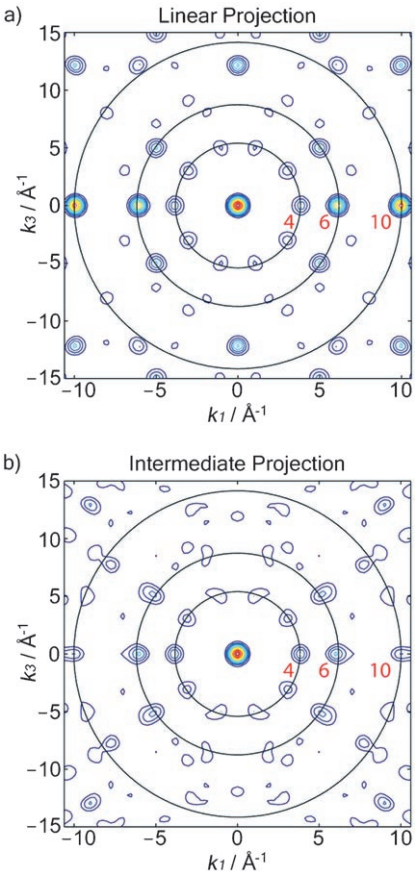

Figure 13. 2D cross-section of the Fourier transforms of a) a linear projection and b) an intermediate projection of the 54-cluster viewed along the $[1\bar{1}0]$ direction. These cross-sections contain points of the form $k_1k_1k_3$. IT-IT distances of 2.40 and 2.03 Å were assumed in order that the $(k_1\bar{k_1}0)$ planes divide the 54-cluster into k_1 segments, as in Figure 14. Both plots are divided into 12 equally spaced contours, in which redder lines represent greater constructive interference, and bluer lines less.

Let us consider real space pictures, based at first just on a linear projected 54-cluster, which correspond to these major peaks. In Figure 14a, we show a picture of the 54-cluster

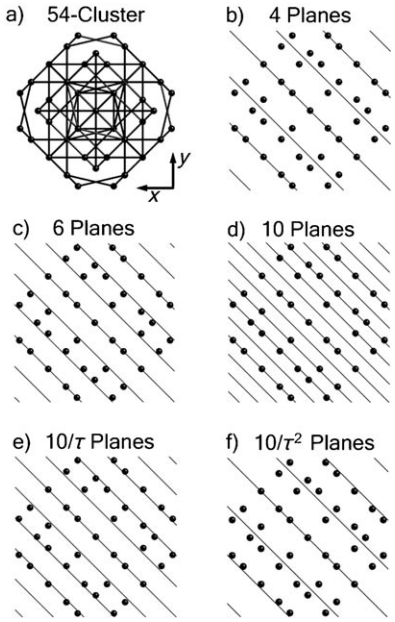

Figure 14. a) A linear projection of the 54-cluster, shown with an OC–OC distance equal to b) 4, c) 6, d) 10, e) $10/\tau$, and f) $10/\tau^2$ (in which τ is the golden mean) spacings of plane waves whose reciprocal lattice vectors are $(k_1\bar{k_1}0)$. Diagonal lines represent the crests of the respective plane waves. The cluster achieves significant constructive interference with the waves at each of the illustrated sizes.

with bonds represented as line segments. In Figure 14b–d, we show this same cluster, but with all the bonds removed for visual clarity. In addition, we show plane waves, the reciprocal lattice vectors of which are $(k_1\bar{k}_1 0)$, partitioning the 54-cluster into 4, 6, and 10 segments, respectively. (More exactly, the projected 54-cluster OC–OC distance is chosen to be respectively 4, 6, or 10 times the plane-wave wavelength.)

It can be seen that there is a correspondence between these three $(k_1\bar{k}_1 0)$ plane waves and the projected 54-cluster. In all three cases, the vertices of the 54-cluster lie near the crests of the plane waves. These three wavelengths lead to excellent intracluster constructive interference, and hence strong diffraction peaks. In the case in which the projected 54-cluster OC–OC distance is ten times the wavelength (Figure 14d), constructive interference is nearly ideal.

Numbers such as 4, 6, and 10 are of interest. In particular, if we divide these numbers by two, they correspond to integers in the Fibonacci sequence (1, 1, 2, 3, 5, 8, …). The 54-cluster has the remarkable property that interatomic spacings are related to the Fibonacci sequence. This remarkable property can be directly traced to the 600-cell itself.

The Fibonacci sequence is furthermore naturally connected to the golden mean ($\tau=(1+\sqrt{5})/2$): ratios of adjacent members of the Fibonacci sequence quickly converge to the golden mean. In Figure 14b,c,e,f, we compare plane waves for which the cluster is 6 and 4 times the wavelength to plane waves for which the cluster is $10/\tau$ (6.18) and $10/\tau^2$ (3.82) times the wavelength, respectively. (We choose ratios related to 10 because for this integer value, constructive interference is already nearly ideal.) As Figure 14e,f show, these two non-integer values have excellent constructive interference.

We quantitatively evaluate the relation of the $10/\tau$ and $10/\tau^2$ wavelengths in the original Figure 13. Recalling that for plane waves, the wavelength λ determines the length of $\vec{k}$ ($\lambda|\vec{k}|=1$), we directly place onto Figure 13 circles, the radii of which correspond to the plane waves labeled 10, $10/\tau$, and $10/\tau^2$ in Figure 14. The three rings labeled 10, 6, and 4 in Figure 13 actually correspond to the 10, $10/\tau$ (6.18), and $10/\tau^2$ (3.82) plane waves, respectively, of Figure 14. Re-examination of Figure 13a shows that the calculated peak maxima lie almost exactly on the calculated ring positions. (By contrast, had we placed plane waves corresponding to wavelengths of either 4.00 or 6.00, we would have seen a significant misalignment between ring sizes and diffraction peak maxima.)

In Figure 13b, the illustrated 10-, 6-, and 4-rings were created in an identical manner, but for an intermediate projected 54-cluster.[14] Comparison of Figure 13a,b shows that ideal constructive interference depends much more on the values 10, $10/\tau$, and $10/\tau^2$ than on the projection method used. It is these wavelengths and the subtle regularities of the 600-cell, rather than the projection method, that are responsible for optimal intracluster constructive interference.

These facts are of central relevance to the paper. In particular, these results suggest that if one were to have a pair of 54-clusters of different sizes, but with a size ratio between clusters of either τ or τ^2, one might have not just optimal intracluster interference, but intercluster interference as well. In Figure 15, we show two 54-clusters with an intercluster size ratio of τ.

As this figure shows, plane waves can constructively interfere equally well for two different sized 54-clusters, the size ratio of which is near the golden mean. Such pairs of different sized clusters are more fully considered in the penultimate section of this paper. For now, note that different sized clusters are not just a hypothetical musing. Rather as we have previously discussed, different sized 54-clusters the size-ratios of which are near the golden mean are extremely common in the $F\bar{4}3m$ family of structures.

[14] In the intermediate 54-cluster, two IC atoms which lie along the $[1\bar{1}0]$ direction with respect to each other were used to define the 10, $10/\tau$, and $10/\tau^2$ plane-wave wavelengths.

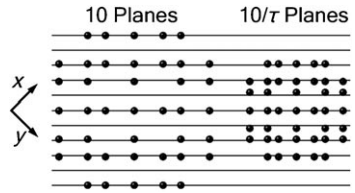

Figure 15. Linear projections of two 54-clusters differing in size by a factor of τ, the golden mean, shown with plane waves, the reciprocal lattice vectors of which are $(k_1\bar{k_1}0)$. Horizontal lines indicate the crests of the plane waves. At these particular sizes, the two clusters can simultaneously achieve significant constructive interference.

3D Bravais space groups compatible with the 54-cluster: In the previous sections of this paper, we found that a single 54-cluster has both T_d and pseudo-fivefold symmetry. There are six pseudo-fivefold axes, each running along one of the edges of the inner tetrahedron (IT) of the 54-cluster. We now determine the crystalline symmetry consequences of the above statements.

First, we assume the symmetry of the actual crystal emanates from the 54-cluster itself: it should be of no higher or no lower symmetry than the 54-cluster's T_d symmetry. We therefore require that the highest symmetry site of the crystal is of T_d symmetry. There are five space groups which meet this requirement: $P\bar{4}3m$, $F\bar{4}3m$, $I\bar{4}3m$, $Pn\bar{3}m$, and $Fd\bar{3}m$. Happily, all the cubic structures which we know to exhibit pseudo-fivefold symmetry along their $\langle 110\rangle$ directions belong to one of these five space groups. These include not just the structures that are the primary concern of this paper, but also the three most complex of all cubic structures: Cd_3Cu_4 ($F\bar{4}3m$),[11] $NaCd_2$ ($Fd\bar{3}m$),[10] and Mg_2Al_3 ($Fd\bar{3}m$).[51,52]

The requirement that the highest site symmetry be T_d not only specifies the possible space groups, but also determines the orientation of the 54-cluster within the cubic unit cell. For a T_d cubic unit cell, the $\bar{4}$ axes always run along the $\langle 100\rangle$ directions, while the threefold axes run in the $\langle 111\rangle$ directions. The edges of the inner tetrahedron define the *m* setting (the third setting, the $\langle 110\rangle$ directions). The edges of the inner tetrahedron therefore must lie in the $\langle 110\rangle$ directions.

As the edges of the inner tetrahedron are the best preserved pseudo-fivefold symmetry axes of the 54-cluster, the most clear pseudo-fivefold symmetry axes lie along the six $\langle 110\rangle$ directions. This is the exact result that we set out to rationalize at the beginning of this paper. Every indication is therefore that the construction of the 4D 600-cell and its projection, the 54-cluster, plays a critical role in the observed pseudo-tenfold diffraction patterns.

Crystalline 54-cluster interference: However, we can go further. Let us consider a single crystallographically inequivalent 54-cluster, and let us place it into a cubic unit cell. As

the crystal structures that interest us are all *F*-centered, we make the unit cell *F*-centered. We now specify the size of the cluster relative to the size of the unit cell. As a measure of the former, we consider the IT–IT distance (as the 600-cell is a Platonic solid, all nearest-neighbor distances are originally the same, and therefore all nearest-neighbor distances initially equal the IT–IT distance). For the latter, we apply the *a*-axis length.

We consider a ratio of *a*-axis/IT–IT distances ranging in value from 3 to 35, and calculate across this range the diffraction pattern. A few of these results are illustrated in Figure 16. (Figure 16 top and bottom are the calculated diffraction patterns for a linear and an intermediate projected 54-cluster, respectively. The results presented in this figure use the same delta-function-like atomic form factors as were used for the isolated 54-clusters.) All ratios calculated exhibit a pseudo-tenfold diffraction. Thus, the size ratio is not a factor in the overall pseudo-fivefold symmetry (this is as we would expect: the pseudo-fivefold symmetry is a consequence of the finite 4D cluster, and is therefore independent of 3D cell axis length).

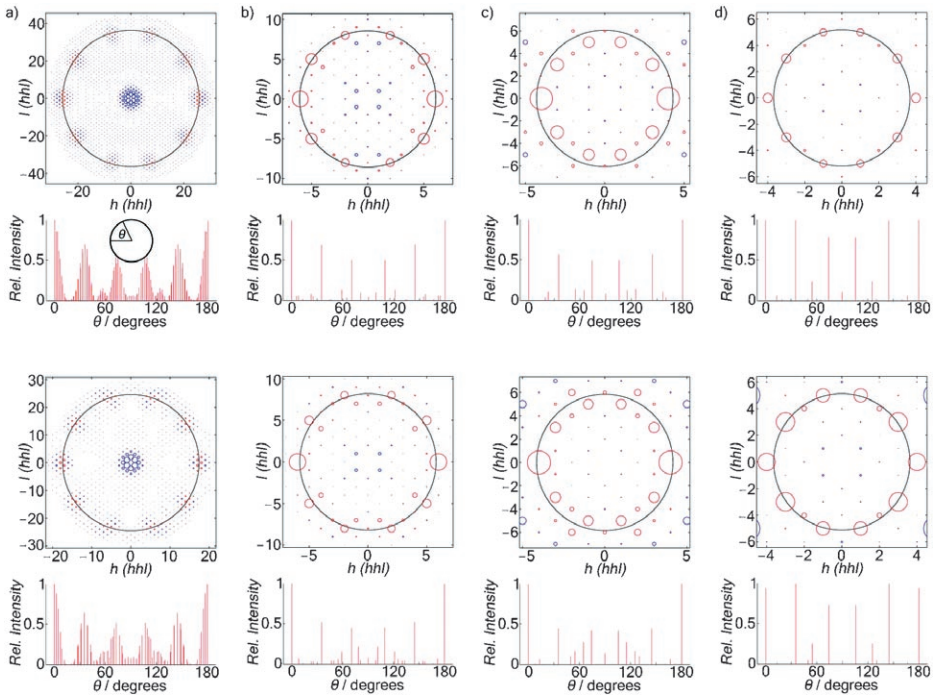

Figure 16. 2D (blue and red) and circular 1D (red) diffraction patterns for linear (top row) and intermediate (bottom row) projections of the 54-cluster placed in an *F*-centered cubic cell, illustrating the dependence of peak sharpness on the relative sizes of the unit cell and the cluster. Unit cell axes of a) 25 (linear) and 20 (intermediate), b) 5.9 (linear) and 6.7 (intermediate), c) 4.2 (linear) and 4.8 (intermediate), d) 3.6 (linear) and 4.2 (intermediate) times the IT–IT distance. A ring corresponding to peak maxima of an isolated 54-cluster (4-ring of Figure 13) is shown as a black circle. For both types of projection, optimal peak sharpness and location (vis-à-vis the 4-ring) is approximately six (panel b) or four (panel d) times the IT–IT distance.

However, even within the constraint of pseudo-fivefold symmetry, there is an enormous variation in diffraction patterns. We observe two trends. First, at the largest ratios, the pseudo-tenfold diffraction peaks are distributed over a number of neighboring *hkl* reflections, but at smaller ratios, the pseudo-tenfold diffraction coalesces into single peaks. A second distinction is also present. As Figure 16 shows, the most intense peaks shift in their positions.

To aid our understanding of these shifts, we place directly onto the diffraction images in Figure 16 a constant ring that corresponds to the 4-diffraction ring previously calculated (for the isolated 54-cluster). As Figure 16 shows, the actual diffraction pattern fluctuates with respect to the isolated cluster ring.

If the diffraction peaks of Figure 16 are not fully in accord with the Fourier transform of the isolated cluster, then there must be a less-than-ideal constructive interference present in the diffraction pattern. Intra- and intercluster planes must not be fully aligned. Constructive interference can only be optimal when the diffraction peaks of Figure 16 lie on the isolated 54-cluster ring positions.

Examination of data across the full range of calculated sizes suggests that for some specific size ratios, there is optimal agreement between isolated and crystalline 54-cluster diffraction patterns. The two best ones are illustrated in Figure 16b,d. The first is found near a size ratio of six, the second near the value of four (the specific optimal value itself shifts somewhat depending on the method of projection). In both of these cases, intense reflections lie directly on the illustrated ring.

A simple metric which could quantitatively evaluate what the naked eye sees would be useful. Such a metric would need two components. On the one hand, it would measure the degree to which peaks coalesce. On the other hand, it would measure the proximity of the coalesced peak to those that were calculated for the isolated 54-cluster. Interestingly, as pseudo-tenfold symmetry appears to play an equal role in all the diffraction images, the desired metric need not measure tenfold symmetry.

A pithy metric proves cumbersome to find. We develop it in two steps. First, we consider the 4-ring of the isolated 54-cluster. Intracluster diffraction is optimal for points along this ring. We now determine which *hkl* peaks lie nearest these optimal values. To do so, we consider the reciprocal lattice itself. The reciprocal lattice has vertices that correspond to specific *hkl*, and edges (connections between neighboring vertices) that might intersect the 4-ring. We

consider only those *hkl* the attached edges of which intersect the 4-ring. The selected *hkl* are shown in red in Figure 16.

At the base of each panel of Figure 16, we show the selected diffraction peaks in a separate graph. These graphs plot the intensities of the selected diffraction peaks as a function of the angles to which they correspond along the ring. As these figures show, for all size-ratios, the diffraction patterns take on a pseudo-tenfold symmetry. There are ten major peaks distributed symmetrically around the ring (six of which are given in the basal pictures); each peak has a number of satellite peaks.

We now establish the first half of the desired metric. We divide the 180° graphs into five cohorts of peaks, each corresponding to a 36° range of peaks. We then select the strongest peak in each cohort (its intensity is called I_1), and take its ratio with respect to the second strongest peak (the intensity of which is I_2). We calculate the geometric mean of these ratios. As by symmetry, these five cohorts always consist of just three sorts, we take the geometric mean of just the three symmetry-inequivalent cohorts. This geometric mean provides a measure of how peaked any given diffraction pattern is.

We now consider the actual position of these strongest five peaks relative to the ring itself. We calculate the distance between the three distinct most intense peaks and a set of three points lying on the illustrated ring with ideal tenfold symmetry, and take the geometric mean of these distances. We now multiply these two geometric means together. This product can be thought of as a measure of the accord between intra- and intercluster constructive interference.

In Figure 17a,b, we plot this product for both a linear and an intermediate projected 54-cluster. In the case of linear projection, there are two strong and sharp peaks at size ratios of 3.9 and 5.8. For intermediate projection, the corresponding values are 4.0 and 6.9. For ease of comparison, we also replot, in Figure 17c, the data based on the actual crystal structures. As we have previously shown, experimentally there are two observed size ratios, the first mainly ranging from 3.5–3.8, the second more sharply peaked at values around 6.6–6.8.

Both projected clusters and the experimental data agree that there are two optimal size ratios, one near 4 and the other near 6. The observed experimental range lies somewhere between the values obtained from the linear and the intermediate projection methods. Perhaps not too surprising, in the case of the smaller cluster (the clusters with size ratios of six), the intermediate projection fares better at quantitative rationalization. For the smaller cluster, the interatomic distances are metal bonds themselves. Intermediate projection, with its more constant bond lengths, is therefore more reasonable than linear projection (see Table 2).

In some ways, however, the results of Figure 17 appear surreal. The calculated results are derived solely from geometrical considerations, the mathematical construction of clusters with optimal constructive fivefold diffraction, while the experimental results are presumably due to the optimization of the Schrödinger equation. The agreement between theory and experiment is therefore curious.

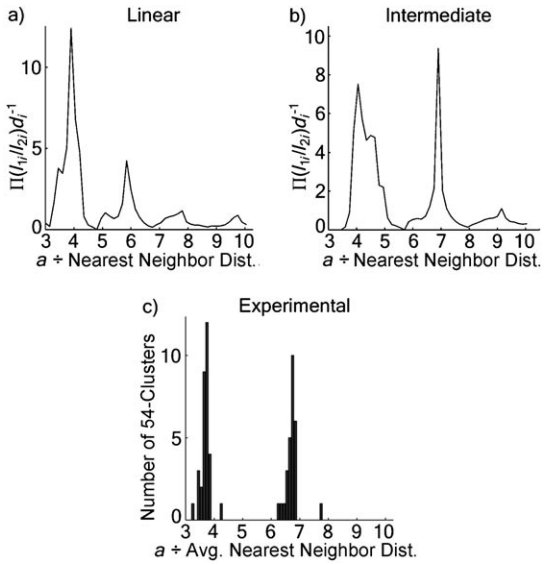

Figure 17. The combined metric (see text) which assesses both the diffraction peak sharpness and peak positions relative to the 4-ring (see Figure 13) for the a) linear and b) intermediate projections of *F*-centered cubic-celled 54-clusters, plotted versus the relative size of the unit cell to the cluster. c) The frequency of each size of 54-cluster in experimental crystal structures. The two distinct ranges of theoretically optimal cluster sizes are matched by experiment.

Fivefold symmetry of multiple 54-clusters: In previous sections of this paper, we found that only at specific length scales does the 54-cluster have its most constructive intracluster interference (Figure 14a–c). We have further suggested that two clusters with different length scales can constructively interfere with one another if their length scales are related by the golden mean (Figure 15).

Crystallographic data for the $F\bar{4}3m$ family of structures (Figure 17c) bears out these theoretical constructions with numerous 54-clusters at two predominant length scales. The length scale of the smaller 54-clusters is dictated by metal bond lengths; the length scale of the larger clusters is larger by a factor of roughly the golden mean. Experimental results are therefore in good agreement with theoretical conjecture.

However, this agreement by itself does not rigorously prove the conjecture. In this penultimate section of the paper, we explicitly calculate the diffraction pattern of two distinct clusters within one unit cell. We consider especially the case in which the two different clusters are centered at different points, as this seemingly could most easily violate real-space pseudo-fivefold symmetry.

As we consider here for the first time the diffraction of two 54-clusters, we must for the first time consider interference effects between two clusters not related by translational symmetry. We need to take into account the orientation of 54-clusters with respect to each other. The 54-cluster ori-

entation is an issue, because this cluster has T_d symmetry. There are two ways to align a tetrahedron with respect to the symmetry of a cubic unit cell, and therefore two ways to orient the 54-cluster. Considering the central IT tetrahedron of the 54-cluster, we can have one of its triangular faces pointing along either the [1 1 1] or [$\bar{1}\,\bar{1}\,\bar{1}$] direction. We shall call the former orientation regular (r or R), and the latter orientation inverted (i or I).

We may then develop the following nomenclature: small and large Roman letters will signify respectively small- and large-sized 54-clusters. R would refer to a large-scaled 54-cluster with the regular orientation. Combining these names with the Z, Q, H, and T notation, we can generate an efficient naming scheme. Qi for example will specify a small-scaled 54-cluster with the inverted orientation, centered at $(\frac{1}{4},\frac{1}{4},\frac{1}{4})$.

In Figure 18a, we consider one regular and one inverted cluster located at respectively Z and Q. (We choose Z and Q because, as Table 4 shows, these are the most common cluster centers.) We calculate the diffraction pattern for cell-to-cluster size ratios ranging from 3 to 35 using the product established in the preceding section to assess the diffraction pattern. As Figure 18a shows, there are a number of optimal size ratios of the two clusters. The globally optimal ratio is for one cluster to have a size ratio of six (i.e., r or i), while the other has a size-ratio of four (i.e., R or I). The second most optimal ratio is for both clusters to have size ratios of four.

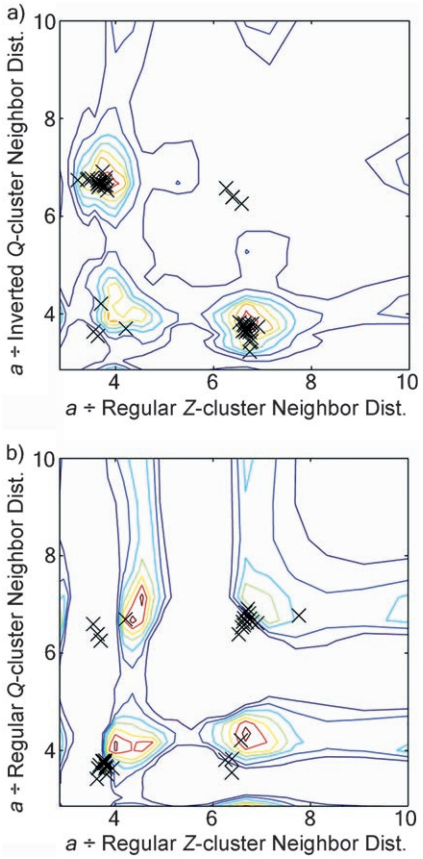

Figure 18. Contour plots of the combined metric (see text) which assesses both diffraction peak sharpness and peak positions relative to the 4-ring (see Figure 13) for *F*-centered cubic unit cells containing the intermediate projections of two 54-clusters centered respectively at Z and Q, a) with clusters with inverted orientation with respect to each other and b) with the same orientation. Both plots are divided into seven equally spaced contours, in which redder lines represent larger values, and bluer lines smaller values. Crosses indicate experimentally observed arrangements of pairs of clusters. See text for discussion.

The figure shows two identical globally optimal peaks. We can apply our nomenclature to verify that they should be identical. The first of the two optimal peaks corresponds to the pair of 54-clusters Zr·QI, while the second is for two clusters ZR·Qi. Now consider the effect on the first two clusters if they are inverted about the point $(\frac{1}{8},\frac{1}{8},\frac{1}{8})$. In this operation, the Z and Q sites switch labels. Furthermore, r and I convert to i and R, respectively. Thus, Zr·QI becomes Qi·ZR, and the aforementioned peaks are symmetry-equivalent. (Note Qi·ZR = ZR·Qi.)

We place, directly on the figure, crosses that correspond to the experimentally determined pairs of clusters. (In addition to pairs of clusters centered at Z and Q, we also include pairs of clusters located at Q and H, H and T, or T and Z sites. We do so because the calculated contour maps are equally valid for all pairs of neighboring centers.) Agreement between theory and experiment is good. The largest number of peaks is found at Zr·QI and ZR·Qi. In addition, there are a few experimentally observed points that lie near the second most optimal geometry, ZR·QI, and three points at Zr·Qi (the presence of these last points is the subject of the last paragraph in this section).

We now turn to the cases of Zr·Qr, Zr·QR, ZR·Qr, and ZR·QR. We examine these cases in light of our earlier observations for the Zr·QI peaks. We first note two geometrical issues. First, we observe that one cannot have Zr and ZR clusters simultaneously in the same crystal structure. This is because the ZIT atom provides the IT site of the Zr cluster, but ZOT provides not just the OT site of the Zr cluster but the IT site of the ZR cluster. In a 54-cluster, the IT tetrahedron has one orientation, while the OT tetrahedron has the opposite orientation. Thus the ZOT site cannot simultaneously be the OT site of a Zr cluster and the IT site of a ZR cluster.

Second, we note Zr and Zi are not compatible. In Zr, we would have a regularly oriented IT and therefore an inverted OT, while in Zi we would have an inverted IT and regularly oriented OT. Zr and Zi are not compatible, as an inverted (or regular) OT and an inverted (or regular) IT would lie too close to one another to be simultaneously present. (For a similar reason, QI and QR are not found together.)

These two geometrical observations place considerable constraints on the Zr·Zr, Zr·ZR, ZR·Zr, and ZR·ZR peaks. As we have seen in Figure 18a, the Zr·QI configuration is quite common. If the crystal in question has the Zr·QI configuration, then the presence of Zr and QI rules out the presences of respectively Zi or ZR and Qi or QR. (Qi and QI can not be simultaneously present for the same reason Zr

and ZR can not be simultaneously present.) However ZI and Qr are compatible with Zr and QI. Since we are at this point interested in a pair of clusters with the same orientation, the only admissible possibilities would be Zr·Qr and ZI·QI. We further note that following inversion, ZI·QI becomes ZR·QR.

We therefore expect that as Zr·QI is quite common, the two most common orientations among Zr·Qr, Zr·QR, ZR·Qr, and ZR·QR would be Zr·Qr and ZR·QR. The experimental data of Figure 18b confirm this hypothesis. The majority of experimental data is for these two cluster pairs, with a few Zr·QR cluster pairs also present.

The experimental data is therefore compatible with the theoretical calculations. We end this section, however, with one caveat. The theoretical calculations do not unambiguously anticipate the experimental results. There is one additional possibility compatible with theory that is not most commonly observed. It could have been that Zr·QR (rather than Zr·QI) was most commonly observed. ZI and Qi are compatible with Zr·QR. As a consequence, ZI·QR and Zr·Qi would also have been seen. This second possibility is what allows for the experimental pairs that lie off the global maxima of Figure 18.

Conclusions

In this paper, we have shown that the pseudo-fivefold symmetries of a number of complex solid-state compounds can be understood by considering the higher dimensional Platonic solid, the 600-cell. In the preface to his classic work on higher dimensional Platonic solids, *Regular Polytopes*, H. S. M. Coxeter talks of the dazzling beauty of 4D solids. He quotes Lobatschewsky, who wrote, "there is no branch of mathematics, however abstract, which may not some day be applied to phenomena of the real world."[46] Solid-state chemists are blessed that it is in our field in which such dazzling and beautiful mathematical constructs as the 600-cell can take hold.

In some ways it is not an accident. One of the central concerns of solid-state chemists is the filling of space with polyhedra. Furthermore, most binary compounds are metals, and their structures are often built up of tetrahedra. The complexity of many crystal structures is a consequence of these statements. For, as we know, it is not possible to fill space solely with regular tetrahedra.

We may think of the intrusion of the 4D 600-cell into solid-state chemistry as a consequence of the above. Just as the exterior of a 3D polyhedron is a curved 2D surface, the exterior of a 4D polyhedroid is a curved 3D volume.[15] But what a volume! Every vertex is in the center of an icosahedron, each icosahedron is composed of 20 perfectly regular tetrahedra, and all faces of all tetrahedra lie on the face of an adjacent tetrahedron. Were such an object to exist in ordinary 3D space, we would reasonably expect that there would be numerous phases which would adopt its structure. Even in curved space, we can imagine (and we hope in this paper have shown) such a geometrical object is of use.

However, at the same time, we view the 600-cell as just a point of departure. We suspect its point group and representations of its point group will also play a significant role in the understanding of complex intermetallic structures. The point group of the 600-cell has 14400 elements; its irreducible representations are of a complexity far beyond those encountered in 3D point groups. The utility of the point group and its representations in simplifying and classifying solutions to the Schrödinger equation is well known.

The 600-cell is just one of many geometrical objects that belong to this point group. In a previous paper, we have described an edge-capped stella quadrangula, the edges of which are decorated with new atoms.[39] In an analogous manner, we can envision decorated 600-cells. However, the 600-cell point group may have more far-reaching consequences; just as regular quasicrystals have I_h point-group symmetry,[1] we may envision new quasicrystals that belong to the 600-cell point group.[53] Such further constructs seem worthy of investigation.

Appendix

Linear projection of the 16-cell: The eight vertices of the 16-cell can be described in Cartesian coordinates by $(\pm1,0,0,0)$, $(0,\pm1,0,0)$, $(0,0,\pm1,0)$, and $(0,0,0,\pm1)$. In 4D, each vertex is distance 1 from the origin, and has six nearest neighbors at a distance of $\sqrt{2}$. To find the matrix that creates a linear 3D projection of the 16-cell, we must define the direction of projection. As discussed earlier in this article, we chose the direction of projection to be orthogonal to the central tetrahedron (thus preserving the symmetry of this tetrahedron). We arbitrarily chose the central tetrahedron to have vertices at (1,0,0,0), (0,1,0,0), (0,0,1,0), and (0,0,0,1). We would like these four points to be projected onto the vertices of a 3D tetrahedron, the vertices of which we (again somewhat arbitrarily) place at (−1,−1,−1), (−1,1,1), (1,−1,1), and (1,1,−1). The desired projection matrix M_{16} can now be found by solving the system of linear equations represented by

$$M_{16}\begin{pmatrix}1&0&0&0\\0&1&0&0\\0&0&1&0\\0&0&0&1\end{pmatrix}=\begin{pmatrix}-1&-1&1&1\\-1&1&-1&1\\-1&1&1&-1\end{pmatrix}$$

The solution to this system of equations is

$$M_{16}=\begin{pmatrix}-1&-1&1&1\\-1&1&-1&1\\-1&1&1&-1\end{pmatrix}\begin{pmatrix}1&0&0&0\\0&1&0&0\\0&0&1&0\\0&0&0&1\end{pmatrix}^{-1}=\begin{pmatrix}-1&-1&1&1\\-1&1&-1&1\\-1&1&1&-1\end{pmatrix}$$

When the matrix M_{16} is applied to the 4D coordinates of the eight vertices of the 16-cell, the result is a 3D projection with T_d symmetry.

$$M_{16}\begin{pmatrix}1&0&0&0&-1&0&0&0\\0&1&0&0&0&-1&0&0\\0&0&1&0&0&0&-1&0\\0&0&0&1&0&0&0&-1\end{pmatrix}=\begin{pmatrix}-1&-1&1&1&1&1&-1&-1\\-1&1&-1&1&1&-1&1&-1\\-1&1&1&-1&1&-1&-1&1\end{pmatrix}$$

[15] Both the 2D exterior surface of the 3D polyhedra and the 3D exterior volume of a 4D polyhedroid are curved, as the individual exterior elements (respectively 2D polygons and 3D polyhedra) are canted with respect to each other so that they can wrap around the respectively 3D and 4D spaces.

The attentive reader may notice that this 3D projection of the 16-cell is actually a cube. Therefore, while our method did not require it, this projection has O_h symmetry, of which T_d is a subgroup. While one of course does not need four dimensions to generate a cube, this method can be applied to more complicated 4D polyhedroids for which projection proves more useful.

Linear projection of the 600-cell: We now use this same method to generate a 3D projection of the 600-cell with T_d symmetry. The 120 vertices of the 600-cell can be described in Cartesian coordinates by $(\pm\frac{1}{2},\pm\frac{1}{2},\pm\frac{1}{2},\pm\frac{1}{2})$ (16 vertices), $(0,0,0,\pm1)$ (8 vertices), and all even permutations of $^1/_2(\pm1,\pm\tau,\pm\frac{1}{\tau},0)$ (96 vertices, τ is the golden mean). In 4D, each vertex is distance 1 from the origin, and has twelve nearest neighbors at a distance of $\frac{1}{\tau}$. We arbitrarily chose the central tetrahedron to consist of the four mutually nearest neighboring vertices at $(1,0,0,0)$, $^1/_2(\tau,0,\frac{1}{\tau},1)$, $^1/_2(\tau,1,0,\frac{1}{\tau})$, and $^1/_2(\tau,\frac{1}{\tau},1,0)$. We would again like these four points to be projected onto $(-1,-1,-1)$, $(-1,1,1)$, $(1,-1,1)$, and $(1,1,-1)$ in 3D space. The desired projection matrix M_{600} can now be found by solving the system of linear equations represented by

$$M_{600}\begin{pmatrix} 1 & \tau/2 & \tau/2 & \tau/2 \\ 0 & 0 & 1/2 & 1/2\tau \\ 0 & 1/2\tau & 0 & 1/2 \\ 0 & 1/2 & 1/2\tau & 0 \end{pmatrix}=\begin{pmatrix} -1 & -1 & 1 & 1 \\ -1 & 1 & -1 & 1 \\ -1 & 1 & 1 & -1 \end{pmatrix}$$

The solution to this system of equations is

$$M_{600}=\begin{pmatrix} -1 & -1 & 1 & 1 \\ -1 & 1 & -1 & 1 \\ -1 & 1 & 1 & -1 \end{pmatrix}\begin{pmatrix} 1 & \tau/2 & \tau/2 & \tau/2 \\ 0 & 0 & 1/2 & 1/2\tau \\ 0 & 1/2\tau & 0 & 1/2 \\ 0 & 1/2 & 1/2\tau & 0 \end{pmatrix}^{-1}=\begin{pmatrix} -1 & 1+2\tau & 1 & -1 \\ -1 & -1 & 1+2\tau & 1 \\ -1 & 1 & -1 & 1+2\tau \end{pmatrix}$$

Applying this matrix M_{600} to the 4D coordinates of the 600-cell produces a 3D projection of the polyhedroid with T_d symmetry. The full list of 4D and 3D coordinates of the 600-cell under this linear projection are given in the Supporting Information. In the second column of Table 5 are the 3D coordinates of the seven distinct sites in the 54-cluster discussed in this paper, as projected linearly from the 600-cell.

Stereographic and intermediate projections of the 600-cell: Having already found the T_d linear projection of the 600-cell, we must stretch or shrink regions of that projection in order to generate the stereographic and intermediate projections. As with the linear projection, we would like the vertices $(1,0,0,0)$, $^1/_2(\tau,0,\frac{1}{\tau},1)$, $^1/_2(\tau,1,0,\frac{1}{\tau})$, and $^1/_2(\tau,\frac{1}{\tau},1,0)$ to form a tetrahedron at the center of these projections. This means positioning the "light" opposite the center of this tetrahedron, in the direction $\{-(\tau+1,\tau-1,\tau-1,\tau-1)\}/(2\sqrt{2})$. We define γ as the distance from the point on the 600-cell at the center of the projection to the "light", in 600-cell diameters. Thus, a stereographic projection corresponds to $\gamma=1$, the intermediate projection we use in this paper corresponds to $\gamma=1.9$, and a linear projection corresponds to $\gamma=\infty$. We can now calculate the projected 3D coordinates (b_1,b_2,b_3) of any 4D vertex (a_1,a_2,a_3,a_4) for any value of γ.

$$\begin{pmatrix} b_1 \\ b_2 \\ b_3 \end{pmatrix}=\frac{M_{600}\begin{pmatrix} a_1 \\ a_2 \\ a_3 \\ a_4 \end{pmatrix}}{2\gamma-1+\frac{(\tau+1\quad \tau-1\quad \tau-1\quad \tau-1)}{2\sqrt{2}}\begin{pmatrix} a_1 \\ a_2 \\ a_3 \\ a_4 \end{pmatrix}}$$

As a final step, not shown in the above expression, we multiply all the 3D coordinates by a constant such that the IT coordinates are $(-1,-1,-1)$, $(-1,1,1)$, $(1,-1,1)$, and $(1,1,-1)$, so they can be more easily compared. In the third and fourth columns of Table 5 are the seven distinct sites in the 54-cluster, as projected from the 600-cell with $\gamma=1$ (stereographic) and $\gamma=1.9$ (intermediate). As expected, the outer layers of the cluster are more stretched out as the projection moves closer to stereographic.

Table 5. 3D coordinates of various projections of the 600-cell.

Cluster site	Linear ($\gamma=\infty$)	Stereographic ($\gamma=1$)	Intermediate ($\gamma=1.9$)
IT	(−1.000,−1.000,−1.000)	(−1.000,−1.000,−1.000)	(−1.000,−1.000,−1.000)
OT	(1.618,1.618,1.618)	(1.740,1.740,1.740)	(1.679,1.679,1.679)
OH	(0.000,0.000,3.236)	(0.000,0.000,3.650)	(0.000,0.000,3.439)
CO	(−0.618,−2.618,−2.618)	(−0.757,−3.207,−3.207)	(−0.683,−2.894,−2.894)
IC	(1.618,1.618,3.618)	(2.302,2.302,5.147)	(1.914,1.914,4.279)
MC	(−4.236,−1.000,−1.000)	(−6.694,−1.580,−1.580)	(−5.236,−1.236,−1.236)
OC	(−2.618,−2.618,−2.618)	(−4.442,−4.442,−4.442)	(−3.329,−3.329,−3.329)

Acknowledgements

This research was supported by the National Science Foundation through grant DMR-0504703. We thank Dr. Ji Feng for suggesting stereographic projection. We thank Aaron Bloomfield, Julie Fichot, and Adrian So for their separate work in our laboratory on the $Li_{21}Si_5$ structure. We thank Roald Hoffmann for his support through every stage of this work: from discussions over the ideas behind this paper to the final preparation of the manuscript.

[1] C. Janot, *Quasicrystals: A Primer*, 2nd ed., Clarendon, Oxford, **1994**.
[2] G. Friedel, *C. R. Hebd. Seances Acad. Sci.* **1913**, *157*, 1533–1536.
[3] J. Kasper, *Theory of Alloy Phases*, American Society of Metals, Cleveland, OH, **1956**.
[4] F. Frank, J. Kasper, *Acta Crystallogr.* **1958**, *11*, 184–190.
[5] F. Frank, J. Kasper, *Acta Crystallogr.* **1959**, *12*, 483–499.
[6] W. Pearson, C. Shoemaker, *Acta Crystallogr. Sect. B* **1969**, *25*, 1178–1183.
[7] C. Shoemaker, D. Shoemaker, *Acta Crystallogr. Sect. B* **1972**, *28*, 2957–2965.
[8] Y. Yarmolyuk, P. Kripyakevich, *Kristallografiya* **1974**, *19*, 539–545.
[9] D. Shoemaker, C. Shoemaker, *Acta Crystallogr. Sect. B* **1986**, *42*, 3–11.
[10] S. Samson, *Nature* **1962**, *195*, 259–262.
[11] S. Samson, *Acta Crystallogr.* **1967**, *23*, 586–600.
[12] S. Samson, D. Hansen, *Acta Crystallogr. Sect. B* **1972**, *28*, 930–935.
[13] S. Samson, *Acta Crystallogr. Sect. B* **1972**, *28*, 936–945.
[14] V. Khare, N. Lalla, R. Tiwari, O. Srivastava, *J. Mater. Res.* **1995**, *10*, 1905–1912.
[15] C. Dong, *Philos. Mag. A* **1996**, *73*, 1519–1528.
[16] V. Demange, J. Ghanbaja, F. Machizaud, J. Dubois, *Philos. Mag.* **2005**, *85*, 1261–1272.
[17] H. Nyman, S. Andersson, *Acta Crystallogr. Sect. A* **1979**, *35*, 580–583.
[18] H. Nyman, S. Andersson, *Acta Crystallogr. Sect. A* **1979**, *35*, 934–937.
[19] B. Hyde, S. Andersson, *Inorganic Crystal Structures*, Wiley, New York, NY, **1989**.
[20] J.-F. Sadoc, *J. Phys. Let.* **1983**, *44*, L707–L715.
[21] J.-F. Sadoc, R. Mosseri, *Geometrical Frustration*, Cambridge University Press, Cambridge, UK, **1999**.
[22] P. Villars, L. Calvert, *Pearson's Handbook of Crystallographic Data for Intermetallic Phases*, 2nd ed., ASM International, Materials Park, OH, **1991**.
[23] R. Ramirez, R. Nesper, H.-G. von Schnering, *Z. Naturforsch. A.* **1986**, *41*, 1267–1282.
[24] R. Nesper, H.-G. von Schnering, *J. Solid State Chem.* **1987**, *70*, 48–57.
[25] A. Johansson, S. Westman, *Acta Chem. Scand.* **1970**, *24*, 3471–3479.

[26] S. Thimmaiah, K. Richter, S. Lee, B. Harbrecht, *Solid State Sci.* **2003**, *5*, 1309–1317.
[27] L. Arnberg, A. Jonsson, S. Westman, *Acta Chem. Scand. Ser.A* **1976**, *30*, 187–192.
[28] M. Booth, J. Brandon, R. Brizard, C. Chieh, W. Pearson, *Acta Crystallogr. Sect. B* **1977**, *33*, 30–36.
[29] L. Westin, *Chem. Scr.* **1971**, *1*, 127–135.
[30] A. Koster, J. Schoone, *Acta Crystallogr. Sect. B* **1981**, *37*, 1905–1907.
[31] L. Westin, L.-E. Erdshammar, *Acta Chem. Scand.* **1972**, *26*, 3619–3626.
[32] S. Lidin, M. Jacob, A.-K. Larsson, *Acta Crystallogr. Sect. C* **1994**, *50*, 340–342.
[33] F. Bonhomme, K. Yvon, *J. Alloys Compd.* **1995**, *227*, L1–L3.
[34] W. Hornfeck, S. Thimmaiah, S. Lee, B. Harbrecht, *Chem. Eur. J.* **2004**, *10*, 4616–4626.
[35] V. Smetana, V. Babizhetskyy, G. Vajenine, A. Simon, *Angew. Chem.* **2006**, *118*, 6197–6200; *Angew. Chem. Int. Ed.* **2006**, *45*, 6051–6053.
[36] S. Mahne, B. Harbrecht, *J. Alloys Compd.* **1994**, *203*, 271–279.
[37] A. Bradley, P. Jones, *J. Inst. Met.* **1933**, *51*, 131–162.
[38] C. Gazzara, R. Middleton, R. Weiss, E. Hall, *Acta Crystallogr.* **1967**, *22*, 859–862.
[39] R. Berger, S. Lee, R. Hoffmann, *Chem. Eur. J.* **2007**, 7852–7863.
[40] T. Nasch, W. Jeitschko, *J. Solid State Chem.* **1999**, *143*, 95–103.
[41] M. Fornasini, B. Chabot, E. Parthé, *Acta Crystallogr. Sect. B* **1978**, *34*, 2093–2099.
[42] Cerius2, version 3.8, Molecular Simulations, San Diego, CA, **1998**.
[43] H. Manning, *Geometry of Four Dimensions*, Macmillan, New York, NY, **1914**.
[44] E. Jouffret, *Traité Elémentaire de Géométrie à Quatre Dimensions et Introduction à la Géométrie à n-Dimensions*, Gauthier-Villars, Paris, **1903**.
[45] I. Stringham, *Am. J. Math.* **1880**, *3*, 1–14.
[46] H. Coxeter, *Regular Polytopes*, 3rd ed., Dover, New York, NY, **1973**.
[47] M. Kléman, J.-F. Sadoc, *J. Phys. Lett.* **1979**, *40*, L569–L574.
[48] D. Nelson, M. Widom, *Nucl. Phys. B* **1984**, *240*, 113–139.
[49] T. Banchoff, *Beyond the Third Dimension*; Scientific American Library, New York, NY, **1990**.
[50] M. Ladd, R. Palmer, *Structure Determination by X-ray Crystallography*, 2nd ed., Plenum, New York, NY, **1985**.
[51] S. Samson, *Acta Crystallogr.* **1965**, *19*, 401–413.
[52] M. Feuerbacher, *Z. Kristallogr.* **2007**, *222*, 259–288.
[53] V. Elser, N. Sloane, *J. Phys. A* **1987**, *20*, 6161–6168.

Received: September 5, 2007
Published online: March 17, 2008

